Development of computational small animal models and their applications in preclinical imaging and therapy research

Xie, Tianwu; Zaidi, Habib

How to cite

XIE, Tianwu, ZAIDI, Habib. Development of computational small animal models and their applications in preclinical imaging and therapy research. In: Medical physics, 2016, vol. 43, n° 1, p. 111–131. doi: 10.1118/1.4937598

This publication URL: https://archive-ouverte.unige.ch/unige:90684
Publication DOI: 10.1118/1.4937598

Development of computational small animal models and their applications in preclinical imaging and therapy research

Tianwu Xie
Division of Nuclear Medicine and Molecular Imaging, Geneva University Hospital, Geneva 4 CH-1211, Switzerland

Habib Zaidi[a)]
Division of Nuclear Medicine and Molecular Imaging, Geneva University Hospital, Geneva 4 CH-1211, Switzerland; Geneva Neuroscience Center, Geneva University, Geneva CH-1205, Switzerland; and Department of Nuclear Medicine and Molecular Imaging, University of Groningen, University Medical Center Groningen, Groningen 9700 RB, The Netherlands

(Received 7 July 2015; revised 4 November 2015; accepted for publication 16 November 2015; published 22 December 2015)

The development of multimodality preclinical imaging techniques and the rapid growth of realistic computer simulation tools have promoted the construction and application of computational laboratory animal models in preclinical research. Since the early 1990s, over 120 realistic computational animal models have been reported in the literature and used as surrogates to characterize the anatomy of actual animals for the simulation of preclinical studies involving the use of bioluminescence tomography, fluorescence molecular tomography, positron emission tomography, single-photon emission computed tomography, microcomputed tomography, magnetic resonance imaging, and optical imaging. Other applications include electromagnetic field simulation, ionizing and nonionizing radiation dosimetry, and the development and evaluation of new methodologies for multimodality image coregistration, segmentation, and reconstruction of small animal images. This paper provides a comprehensive review of the history and fundamental technologies used for the development of computational small animal models with a particular focus on their application in preclinical imaging as well as nonionizing and ionizing radiation dosimetry calculations. An overview of the overall process involved in the design of these models, including the fundamental elements used for the construction of different types of computational models, the identification of original anatomical data, the simulation tools used for solving various computational problems, and the applications of computational animal models in preclinical research. The authors also analyze the characteristics of categories of computational models (stylized, voxel-based, and boundary representation) and discuss the technical challenges faced at the present time as well as research needs in the future. [http://dx.doi.org/10.1118/1.4937598]

Key words: small animals, computational models, simulations, Monte Carlo, dosimetry

1. INTRODUCTION

Laboratory animals were extensively used in preclinical experiments to assess the potential of novel molecular imaging probes, exposure–response relationship to investigate different types of ionizing and nonionizing radiations, and to develop and test new medical imaging technologies and instruments. This worthwhile effort aims to support translational research "from mouse to man," which proved to be useful for many applications. In this context, various simulation tools were developed to simulate radiation transport (such as photons, electrons, microwave, and visible light) in realistic computational anthropomorphic animal models mimicking the behavior of diverse medical imaging modalities including bioluminescence tomography (BLT), fluorescence molecular tomography (FMT), single-photon emission computed tomography (SPECT), positron emission tomography (PET), x-ray computed tomography (CT), and magnetic resonance imaging (MRI).[1,2] Depending on the study design and targeted objectives, the simulated results could predict the performance of novel designs of medical imaging instruments before to the construction of costly prototypes, provide the amount and distribution pattern of energy deposited in biological tissues for both ionizing/and nonionizing radiation dosimetry calculations, and simulated datasets for developing new image reconstruction and processing algorithms for the various multimodality imaging platforms. In all applications, accurate anatomical and physiological modeling of laboratory animals is fundamental for performing such simulations.[3,4]

Computational models can be defined using equation-based mathematical functions (stylized models), digital volume arrays (voxel-based models), or boundary representation methods (BREP models). Stylized models use simplified mathematical equations, such as planar, cylindrical, conical, elliptical, toroidal, and spherical structures, to represent internal organs and the exterior contour. Voxel-based models are represented by matrices of segmented voxels from tomographic images. BREP computational models employ polygon mesh or nonuniform rational B-spline (NURBS)

surfaces[4] to describe the surface contours of organs and tissues. Stylized models have many advantages including simplicity, easy incorporation in simulation codes, and fast calculation but fail to reproduce accurately complex anatomic details. Voxel-based model provides better anatomic authenticity but intrinsically introduce inherent discretization errors in the voxelized representation. In addition, it is difficult to change the shape of internal organs and external contours. BREP models are capable of keeping most anatomic features and are deformable. However, they cannot be directly used in most Monte Carlo simulation tools mostly owing to difficulties encountered during the calculation of intersections of particle trajectories with surfaces.[3]

The survey was performed by searching the literature using well-established scientific resources (PubMed, Web of Science, and Google scholar) using the key words "rat model," "mouse model," and "animal model." We then analyzed the database and selected the computational models from the search results. The searched computational animal models were then sorted in chronicle order. By 2014, over 120 computational animal models have been reported in about 50 scientific papers. These computational models were distributed among 15 species, including mouse, rat, crab, trout, frog, flatfish, canine, bee, deer, duck, earthworm, goat, monkey, pig, and rabbit. Table I summarizes the computational animal models developed since 1994, where anatomical features describe the characteristics of used animal specimen, model number is the number of unique animal models reported in the referenced publication, and imaging modality refers to the imaging technique from which the model is derived. Mouse models, rat models, and models for other animals represent 38%, 46%, and 16% of the total number of models, respectively. The development of such a large number of computational animal models within a short period indicates the growth of preclinical research given that less than ten animal models were developed prior to 2000. As a consequence of the popularity and widespread recognition of computational modeling and simulation as trustworthy research tools, a number of questions were addressed. This includes the degree of realism of computational models, how close they are to the anatomy and physiology of laboratory animals, the effect of various computational models on the simulated results, and what will be the future directions in preclinical research? The answers to these questions require an understanding of the rationale and processes followed for developing computational models and evaluating simulation techniques used in a variety of applications. This review summarizes the historical development of computational animal models during the last 20 years and provides some insight into future directions for their application in preclinical research, namely, radiation dosimetry calculations and imaging physics research.

The rest of this paper is organized into the following sections: Sec. 2 deals with the construction of animal computational models. In Sec. 3, we present the historical development of computational animal models and portray the models available, while Sec. 4 reviews simulation tools making use of the computational models described in Sec. 3 Examples of applications of animal computational models are then discussed in Sec. 5. Finally, in Sec. 6, we draw the main conclusions and consider future trends in Sec. 7.

2. CONSTRUCTION OF COMPUTATIONAL ANIMAL MODELS

Computational models employ solid-geometry shapes to represent exterior and interior anatomical features of organisms that can be assigned multiple physicochemical characteristics, such as tissue density, chemical composition, electric conductivity, relative permittivity, and scattering and absorption coefficients for different types of radiation according to the targeted simulation study. The computational efficiency and geometrical compatibility of the computational phantoms and simulation tools are also considered in the modeling process.

As an example, the anatomical parameters of the left and right lungs of rat as estimated from medical images or animal dissections were used to determine the semiprincipal axes, the semimajor axis, and semiminor axis of the appropriate ellipses which depicts the left lung and right lung in stylized rat model, respectively. The whole lung of the rat model[5] as shown in Fig. 1(a) can be described by the union of two ellipsoids. Figure 1(b) shows the stylized rat lung after subtracting the heart and liver using Boolean operations. Using the same approaches, all internal organs and animal body can be represented by a series of simplified functions which are computationally efficient and geometrically compatible with most simulation tools. However, the approximate description of organs/tissues using quadratic equations overlooks considerable anatomical details and introduces significant anatomical uncertainties to the simulation.

The usage of rectangular cuboids in voxel models enables a direct conversion of medical image data to computational models and facilitates the geometry representation in simulation tools. The construction of voxel models requires a large number of contiguous image data sets derived from high-resolution cryosection images, CT, MRI, or PET scans, that need to be processed further using dedicated segmentation utilities to assign each voxel an ID corresponding to a particular tissue of interest. The tissue identification process during the construction of a voxel model is demanding and can take a significant amount of time when performed manually. A number of supervised and unsupervised automated segmentation techniques have been used to alleviate the task of manual segmentation using image processing software for tissue identification (e.g., 3D-DOCTOR, PHOTOSHOP, and ImageJ). This includes thresholding, variational approaches, statistical learning methods, and techniques based on stochastic modeling.[56] In general, automated segmentation techniques perform well for segmenting the skeleton, outlining organs, and cavity regions but were deemed impractical for the internal structures having similar density and composition. Manual segmentations can be used to define all regions of interest in the animal body but the process is time-consuming and requires excellent knowledge of the anatomy.

TABLE I. Summary of developed computational animal models including information on year of publication, developers' affiliations, anatomical features, model numbers, imaging modality used, model type, and applications involving the use of ionizing and nonionizing radiation.

Year	Developer	Affiliation	Anatomical features	Model number	Imaging modality	Model type	Applications
Mouse							
1994	Hui *et al.* (Ref. 6)	Pacific Northwest Laboratory, USA	25 g nude mouse	1	Anatomic data	Stylized model	Calculation of AF for Y-90
1999	Kennel *et al.* (Ref. 7)	Oak Ridge National Laboratory, USA	30 g mouse	1	Anatomic data	Stylized model	Calculation of absorbed dose for Y-90 and Bi-213
2001	Dhenain *et al.* (Ref. 8)	California Institute of Technology, USA	Mouse embryo	1	MRI	Voxel model	Nonionizing radiation applications
2001	Flynn *et al.* (Ref. 9)	Royal Free and University College Medical School, UK	Mouse	1	Anatomic data	Stylized model	Calculation of organ absorbed dose for I-131 and Y-90
2001	Wang *et al.* (Ref. 10)	Nagoya Institute of Technology, Japan	Mouse	1	MRI	Voxel model	Evaluation of promoting effects of 1.5 GHz digital cellular phones on mouse skin carcinogenesis
2003	Kolbert *et al.* (Ref. 11)	Memorial Sloan-Kettering Cancer Center, USA	25 g female athymic mouse	1	MRI	Voxel model	Calculation of S-values for I-131, Sm-153, P-32, Re-188, and Y-90
2004	Funk *et al.* (Ref. 12)	University of California (San Francisco), USA	20, 30, and 40 g mouse with fixed axes ratios	3	Anatomic data	Stylized model	Calculation of radiation dose to mice and rats for F-18, Tc-99m, Tl-201, In-111, I-123, and I-125
2004	Hindorf *et al.* (Ref. 13)	Lund University, Sweden	24 g mouse	1	Anatomic data	Stylized model	Calculation of S-values for Y-90, I-131, In-111, and Tc-99m
2004	Segars *et al.* (Ref. 14)	Johns Hopkins University, USA	Male C57BL/6 mouse	1	MRI	Hybrid model	Ionizing and nonionizing radiation applications
2005	Miller *et al.* (Ref. 15)	University of Missouri, MO	25 g nude mouse with improved bone marrow model	1	Anatomic data	Stylized model	Calculation of AFs for Y-90, Re-188, Ho-166, Pm-149, Cu-64, and Lu-177
2006	Sato *et al.* (Ref. 16)	Chiyoda Technol Corporation, Japan	Mouse	1	Anatomic data	Stylized model	Calculation of absorbed dose for Y-90
2006	Stabin *et al.* (Ref. 17)	Vanderbilt University, USA	27 g transgenic mouse	1	CT	Voxel model	AFs for electrons (0.1–4) MeV and photons of (0.01–4) MeV
2007	Bitar *et al.* (Ref. 18)	INSERM, France	30 g female athymic nude mouse	1	Cryosection	Voxel model	AFs for monoenergetic electron and photon sources
2007	Dogdas *et al.* (Ref. 19)	University of Southern California, USA	28 g normal nude male mouse	1	PET, CT, and cryosection	Voxel model	Ionizing and nonionizing radiation applications
2009	Zhang *et al.* (Ref. 20)	Chinese Academy of Sciences, China	20 g male BALB/c mouse	1	CT	Voxel model	Ionizing radiation dosimetry
2010	Keenan *et al.* (Ref. 21)	Vanderbilt University, TN	25, 30, and 35 g male C57BL/6 mouse	3	Derived from MOBY (MRI)	Voxel model	Radiation dose for monoenergetic electrons, photons, F-18, P-32, I-124, Y-90, In-111, and Lu-177

TABLE I. (*Continued*).

Year	Developer	Affiliation	Anatomical features	Model number	Imaging modality	Model type	Applications
2010	McIntosh *et al.* (Ref. 22)	Australian Centre for Radiofrequency Bioeffects Research, Australia	30 g ICR and ddY male, 22 g female mouse, 22 g pregnant mouse, and 0.5 g mouse fetus	4	Anatomic data	Voxel model	SARs in radio frequency dosimetry for 900 MHz plane wave
2010	Chow *et al.* (Ref. 23)	University of Toronto, Canada	Mouse	3	CT	Voxel model	Radiation dose from micro-CT
2011	Larsson *et al.* (Ref. 24)	Lund University, Sweden	22, 28, and 34 g male C57BL/6 mouse with tumor model	3	Derived from MOBY (MRI)	Voxel model	AFs for monoenergetic photons and electrons. *S*-values for I-125, I-131, In-111, Lu-177, and Y-90
2011	Mohammadi and Kinase (Ref. 25)	JAEA, Japan	Male C57BL/6 mouse	1	Derived from MOBY (MRI)	Voxel model	Radiation dose for monoenergetic photons, electrons, I-131, Sm-153, Re-188, and Y-90
2011	Zhang *et al.* (Ref. 26)	Beijing Institute of Radiation Medicine, China	28 g mouse	1	Cryosection	Voxel model	Radiation dose from external photon beams (0.01–10) MeV
2013	Xie and Zaidi (Ref. 27)	Geneva University Hospital, Switzerland	Male C57BL/6 mouse with various body sizes	17	Derived from MOBY (MRI)	Voxel model	AFs and *S*-values for C-11, N-13, O-15, F-18, Cu-64, Ga-68, Y-86, and I-124
Rat							
1997	Burkhardt *et al.* (Ref. 28)	Swiss Federal Institute of Technology, Switzerland	Rat	1	MRI	Voxel model	Dosimetric analysis of rats in wireless communications system of 900 MHz frequency
1997	Lapin and Allen (Ref. 29)	Northwestern University, USA	350 g SD rat	1	CT	Voxel model	Nonionizing applications
1999	Mason *et al.* (Ref. 30)	Systems Research Laboratories, USA; Brooks Air Force Base, USA	370 g rat	1	MRI	Voxel model	SARs from implanted temperature probes, heating-sensitive paints, and infrared imaging
1999	Chou *et al.* (Ref. 31)	City of Hope National Medical Center, USA	SD rat	1	CT	Stylized model	SARs in an ellipsoidal rat model from handheld wireless telephones
2000	Watanabe *et al.* (Ref. 32)	Ministry of Posts and Telecommunications, Japan	126, 263, and 359 g Fischer 344 rat	3	CT	Voxel model	SAR distribution in rat models under microwave exposure
2004	Funk *et al.* (Ref. 12)	University of California (San Francisco), USA	200, 300, and 400 g rats with fixed axes ratios	3	Anatomic data	Stylized model	Radiation dose to mice and rats from F-18, Tc-99m, Tl-201, In-111, I-123, and I-125
2004	Konijnenberg *et al.* (Ref. 33)	Tyco Healthcare, The Netherlands	386 g Wistar rat	1	Anatomic data	Stylized model	*S*-values for Y-90, In-111, and Lu-177
2004	Leveque *et al.* (Ref. 34)	Centre National de la Recherche Scientifique, France	Rat	1	CT/MRI	Voxel model	RF dosimetry for rats from 900 MHz GSM mobile phone fields

TABLE I. (*Continued*).

Year	Developer	Affiliation	Anatomical features	Model number	Imaging modality	Model type	Applications
2004	Schönborn *et al.* (Ref. 35)	Swiss Federal Institute of Technology, Switzerland	300 g male Wistar rat and 370 g male SD rat	3	CT/MRI	Voxel model	RF dosimetry for rats exposed to 1.62 GHz microwave
2004	Segars *et al.* (Ref. 14)	Johns Hopkins University, USA	Male Wistar rat	1	MRI	Hybrid model	Ionizing radiation applications
2006	Stabin *et al.* (Ref. 17)	Vanderbilt University, USA	248 g SD rat	1	CT	Voxel model	AFs for monoenergetic electrons and photons
2006	Kainz *et al.* (Ref. 36)	Center for Devices and Radiological Health (CDRH), USA	567, 479, 252, and 228 g SD rat	4	MRI, cryosection	Voxel model	RF dosimetry for rats at 902 or 1747 MHz microwave fields
2006	Lopresto *et al.* (Ref. 37)	ENEA, Italy	Rat	1	Anatomic data	Stylized model	Biological effects in rats following exposure to electromagnetic fields of GSM 1800 system
2008	ICRP (Ref. 38)	ICRP	314 g rat	1	Anatomic data	Stylized model	Dose conversion factors for animals under external exposure to 75 radionuclides
2008	Peixoto *et al.* (Ref. 39)	Universidade Federal de Pernambuco, Brazil	310 g Wistar rat	1	CT	Voxel model	AFs for monoenergetic photons and electrons
2008	Wu *et al.* (Ref. 40)	HUST, China	156 g SD rat	1	Cryosection	Voxel model	Radiation dose to rats under external irradiation of photons
2008	Wang *et al.* (Ref. 41)	Nagoya Institute of Technology, Japan	Pregnant Fischer 344 rat	1	MRI	Voxel model	RF dosimetry for pregnant rats from 1.95-GHz cellular phones
2008	Pain *et al.* (Ref. 42)	Universités Paris 11/Paris 7, France	284 g SD rat	1	MRI	Voxel model	Evaluation of uncertainties on radiotracer accumulation quantitation in beta microprobe studies
2009	Zhang *et al.* (Ref. 43)	HUST, China	156 g Sprague-Dawley rat	1	Cryosection	Hybrid model	Radiological imaging applications
2010	Keenan *et al.* (Ref. 21)	Vanderbilt University, TN	200, 300, 400, 500, and 600 g male Wistar rat	5	Derived from MOBY (MRI)	Voxel model	Radiation dose of monoenergetic electrons and photons and F-18, P-32, I-124, Y-90, In-111, Lu-177
2010	Xie *et al.* (Ref. 5)	HUST, China	156 g SD rat	1	Cryosection	Stylized model	Radiation dose of monoenergetic electrons and photons
2011	Arima *et al.* (Ref. 44)	NICT, Japan	115, 314, and 472 g rat	3	CT	Voxel model	RF dosimetry for rats in 1500-MHz microwave fields
2012	Larsson *et al.* (Ref. 45)	Lund University, Sweden	225, 250, 275, and 300 g Brown Norway rat	4	Derived from MOBY (MRI)	Voxel model	S-values for Y-90 and Lu-177
2012	Xie *et al.* (Ref. 46)	HUST, China	153 g SD rat	1	Cryosection	Voxel model	S-values and dose distributions for Y-90, I-131, Ho-166, and Re-188

TABLE I. (*Continued*).

Year	Developer	Affiliation	Anatomical features	Model number	Imaging modality	Model type	Applications
2013	Xie and Zaidi (Ref. 47)	Geneva University Hospital, Switzerland	Wistar rat at different ages	10	Derived from MOBY (MRI)	Voxel model	Age-dependent small animal internal radiation dosimetry
2013	Xie and Zaidi (Ref. 48)	Geneva University Hospital, Switzerland	Wistar rat with different degrees of emaciation and obesity	7	Derived from MOBY (MRI)	Voxel model	Assessment of the effect of emaciation and obesity on small animal radiation dosimetry
Crab							
2008	ICRP (Ref. 38)	ICRP	754 g crab	1	Anatomic data	Stylized model	Dose conversion factors for animals under external exposure to 75 radionuclides
2013	Caffrey *et al.* (Ref. 49)	Oregon State University, USA	464 g Dungeness crab	1	CT and MRI	Voxel model	Radiation dose of monoenergetic electrons and photons
Trout							
2008	ICRP (Ref. 38)	ICRP	1260 g trout	1	Anatomic data	Stylized model	Dose conversion factors for animals under external exposure to 75 radionuclides
2014	Hess *et al.* (Ref. 50)	Oregon State University, USA	658 g Rainbow trout	1	CT and MRI	Voxel model	Radiation dose of monoenergetic electrons and photons
Frog							
2008	ICRP (Ref. 38)	ICRP	31.4 g frog	1	Anatomic data	Stylized model	Dose conversion factors for animals under external exposure to 75 radionuclides
2012	Kinase *et al.* (Ref. 51)	JAEA, Japan	33.7 g frog	1	Cryosection	Voxel model	Radiation dose of monoenergetic electrons and photons
Flatfish							
2008	ICRP (Ref. 38)	ICRP	1310 g flatfish	1	Anatomic data	Stylized model	Dose conversion factors for animals under external exposure to 75 radionuclides
2013	Caffrey *et al.* (Ref. 52)	Oregon State University, USA	1024 g Pleuronectid flatfish	1	CT and MRI	Voxel model	Radiation dose of monoenergetic electrons and photons
Canine							
2008	Padilla *et al.* (Ref. 53)	University of Florida, FL	24 kg Hound cross	3	CT	Stylized/ hybrid/ voxel model	AFs for photons and electrons
Bee							
2008	ICRP (Ref. 38)	ICRP	0.589 g bee	1	Anatomic data	Stylized model	Dose conversion factors for animals under external exposure to 75 radionuclides

TABLE I. (*Continued*).

Year	Developer	Affiliation	Anatomical features	Model number	Imaging modality	Model type	Applications
Deer							
2008	ICRP (Ref. 38)	ICRP	245 kg deer	1	Anatomic data	Stylized model	Dose conversion factors for animals under external exposure to 75 radionuclides
Duck							
2008	ICRP (Ref. 38)	ICRP	1260 g duck	1	Anatomic data	Stylized model	Dose conversion factors for animals under external exposure to 75 radionuclides
Earthworm							
2008	ICRP (Ref. 38)	ICRP	5.24 g earthworm	1	Anatomic data	Stylized model	Dose conversion factors for animals under external exposure to 75 radionuclides
Goat							
1999	Mason *et al.* (Ref. 30)	Systems Research Laboratories, USA; Brooks Air Force Base, USA	20 kg pigmy goat	1	MRI	Voxel model	SARs from implanted temperature probes, heating-sensitive paints, and infrared imaging
Monkey							
1999	Mason *et al.* (Ref. 30)	Systems Research Laboratories, USA; Brooks Air Force Base, USA	7.1 kg rhesus monkey and a phantom monkey	2	MRI	Voxel model	SAR values from implanted temperature probes, heating-sensitive paints, and infrared imaging
Pig							
2008	Toivonen *et al.* (Ref. 54)	Radiation and Nuclear Safety Authority, Finland	25 kg pig	1	CT and MRI	Voxel model	RF dosimetry for pig from 900 MHz GSM mobile phone fields
Rabbit							
2007	Wake *et al.* (Ref. 55)	National Institute of Information and Communications Technology, Japan	Rabbit	1	CT	Voxel model	RF dosimetry for rabbit exposed to 2.45-GHz microwave

Figure 1(c) shows the voxel model of the rat's lung. The ladder-shaped boundary of the voxel model brings in an inaccurate approximate description of the smooth surface of the real organ and the anatomical fidelity of this model depends on the adopted voxel size and consequently the associated computational burden owing to handling large amounts of data. The rigid structure of the voxel model also makes the adjustment of organ shape and deformation of the

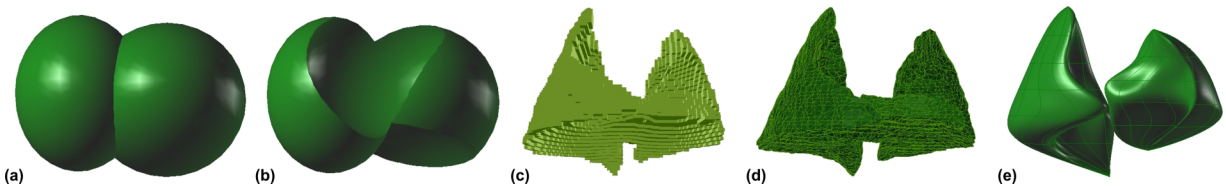

FIG. 1. The rat lung model defined by different methods. (a) The constructive solid-geometry (CSG) model before the subtraction operation. (b) After the subtraction of the heart and liver from the CSG model of the lung. (c) The voxel-based representation of the lung. (d) The lung model represented by polygon mesh. (e) The lung model represented by a NURBS surface.

computational model difficult. The attainable model spatial resolution (voxel size) of voxel-based models is determined by the resolution of the medical imaging modality used to generate them. For micro-MRI, the spatial resolution is about 100–25 μm when using very high strength magnetic fields. For micro-CT, the common spatial resolution is around 50 μm whereas cryosections provide a spatial resolution around 20 μm.

Advanced boundary representation techniques such as the B-splines, NURBS, and polygon meshes can also be used to define organs and animal body. Figure 1(d) shows the developed mesh model of the rat lung using the binary voxel lung model and the marching cubes algorithm of the visualization toolkit (VTK) package. The constructed mesh model can be imported into 3D modeling software such as Autodesk 3ds Max and RHINOCEROS for generating the NURBS model shown in Fig. 1(e). The mesh and NURBS models, collectively referred to as "BREP" model or hybrid model, have smooth contours of organs and provide better anatomical realism than both stylized and voxel models. Hybrid models using NURBS or polygon meshes to represent the surface contours of organs are capable of holding most anatomic characteristics and the flexibility of deforming. However, they cannot be directly adopted within defined geometries of most simulation tools. By voxelizing the deformed hybrid models, one can generate specific voxel models of certain anatomical or physiological characteristics such as tumor-bearing, emaciated, or obese laboratory animals. This customization capability of the hybrid model greatly promoted the concept of computational modeling and simulated the development of dedicated voxel models, thus paving the way for their application in preclinical and clinical radiation dosimetry and medical imaging research.

In summary, stylized models are based on quadratic equations while voxel models make use of tomographic image data. More sophisticated hybrid models are based on advanced surface representations. Figure 2 compares the realism and degree of geometric sophistication of stylized, voxel, and hybrid models developed based on the same rat data set. Figure 3 shows the increasing number of developed computational animal models since 1994. Stylized, voxel, and hybrid models represent 20%, 77%, and 3% of all reported computational animal models, respectively. During the last decade, the total number of computational animal models increased by a factor of 3.3 while the number of voxel models increased by a factor of 5.

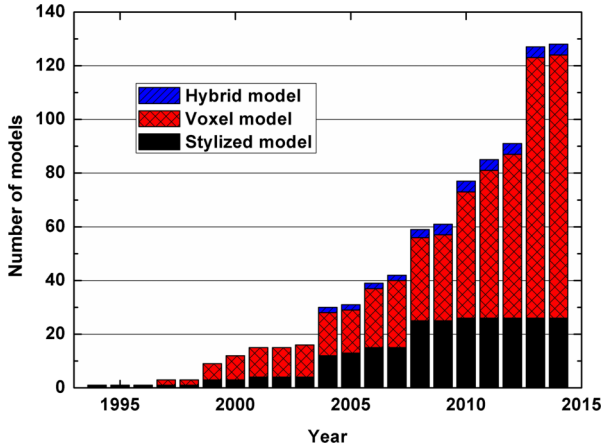

FIG. 3. The increasing number of computational animal models since 1994 demonstrates the growing interest in this area. This graph reflects the number of reported animal models surveyed in Table I.

3. HISTORICAL DEVELOPMENT AND OVERVIEW OF COMPUTATIONAL ANIMAL MODELS

Computational models have evolved from tissue-equivalent ellipsoids homogeneous in composition and density to increasingly realistic models that emulate living organisms in terms of anatomy, composition, and physiology. An understanding of the historical evolution of computational animal models can provide an insight into future development trends. Based on the represented species, currently available computational animal models can be divided into three major categories: (i) mouse models; (ii) rat models; and (iii) models of other animals. In the following, we describe these models in detail.

3.A. Mouse models

The laboratory mouse is the most commonly used mammalian research model in genetics, translational research,

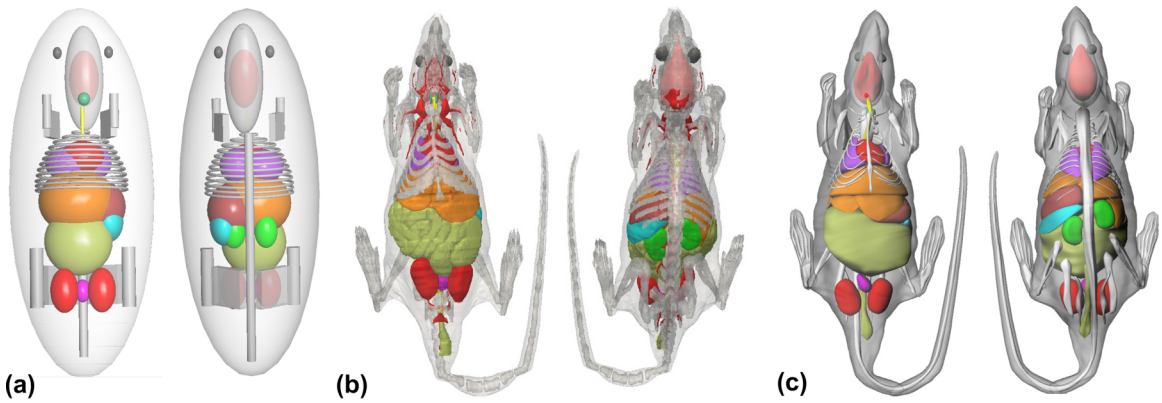

FIG. 2. Ventral–dorsal views (left) and dorsal–ventral views (right) of (a) a stylized rat model, (b) a voxel model with vessels, and (c) a hybrid model.

molecular imaging, radiation dosimetry, and many other scientific disciplines. It has been used extensively to evaluate the biodistribution, pharmacokinetics, radiotoxicity, and effectiveness of novel radiotracers in preclinical research. Radiation dosimetry plays an important role in preclinical research where laboratory animals are used in serial studies with the same animal serving as its own control and, as such, the delivered radiation dose from hybrid imaging devices (e.g., PET/CT or SPECT/CT) might be very high. Although the typical radiation dose levels delivered to small animals during hybrid imaging experiments may not be lethal, they are sufficiently elevated to induce changes in biological pathways that may have an impact on the experimental outcomes.[57] The lethal dose (LD) is the basic quantity used as a dose limitation factor for small animals. The $LD_{50/30}$ (whole-body radiation dose that would kill 50% of the animals exposed to radiation within 30 days) in mice is typically within the range 5–7.6 Gy.[58–60] Typical whole-body radiation doses from micro-CT imaging reported in the literature are within 0.02–0.8 Gy (Refs. 58 and 61) in most of the cases depending on the required image quality, but can go up to 1.5 Gy in cine cardiac micro-CT scanning.[62] Conversely, the radiation dose to mice from nuclear medicine examinations is variable depending on the tracer used and injected activity and mouse size (e.g., 8.9 mGy/MBq for ^{18}F-FDG in a 21 g mouse).[27] In 1994, Hui *et al.*[6] developed the first computational small animal model for reliable estimation of internal doses to laboratory mouse from administered radiotracers and calculated the cross-organ beta doses from Y-90 labeled immunoconjugates. Figure 4 shows the model of Hui *et al.* where the majority of internal organs were modeled as ellipsoids. Henceforward, various computational animal models have been successively reported. Figure 5 shows the representative computational mouse models including the stylized model of Hindorf *et al.*[13] used for estimation of *S*-values for various radionuclides, the voxel-based Digimouse model,[19] and the hybrid MOBY model,[14] the first hybrid mouse model. Kennel *et al.*[7] constructed a 30 g tumor-bearing stylized mouse model whereas Flynn *et al.*[9] developed a stylized mouse model with advanced kidney and tumor models. Other stylized models were also reported in the literature including three stylized mouse models with fixed axis ratios,[12] a stylized mouse model with detailed bone marrow model,[15] a 24 g stylized mouse model enabling the evaluation of parameters influencing the absorbed doses per cumulated activity (*S*-values) in mouse dosimetry,[13] and a stylized mouse model for absorbed dose calculation for Y-90.[16]

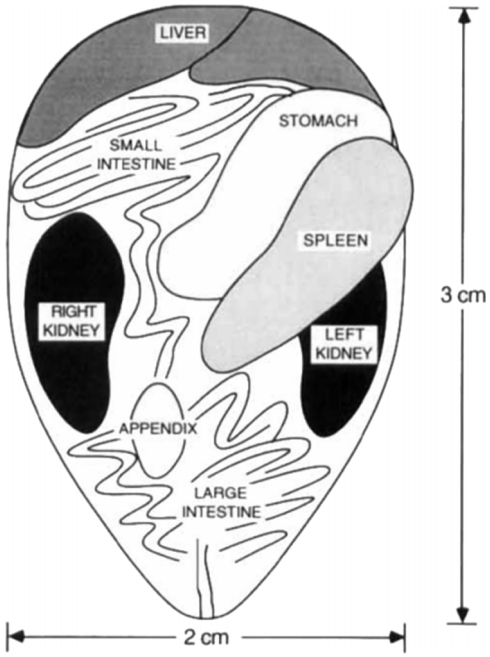

FIG. 4. The first computational animal model developed by Hui *et al.* (Ref. 6) in 1994. [Reproduced with permission from T. E. Hui, D. R. Fisher, J. A. Kuhn, L. E. Williams, and C. Nourigat, "A mouse model for calculating cross-organ beta doses from yttrium-90-labeled immunoconjugates," Cancer **73**, 951–957 (1994). Copyright © 1994 John Wiley and Sons.]

Among the second family of models (voxel-based), Dhenain *et al.*[8] reported on a digital mouse atlas constructed using high-resolution MR images whereas Zhang *et al.*[26] developed a 28 g voxel-based mouse from cryosection image data. A voxel mouse model was developed to study the biological effects of cellular telephones.[10] Chow *et al.* developed three mouse models from CT images of the same mouse generated without (heterogeneous) and with overriding tissue type to soft tissue (homogeneous) and to soft tissue for the bone (bone homogeneous).[23] A number of other voxel-based models were also developed including a 20 g male BALB/c mouse,[20] a 25 g female athymic mouse model and calculated murine *S*-values for the liver, spleen, and kidney,[11] a 27 g transgenic mouse model using CT images,[17] and a 30 g female athymic nude mouse built from cryosection image data.[18] Dogdas *et al.*[19] developed the well-known and widely used voxel-based Digimouse model from CT, cryosection, and PET images of a 28 g nude male mouse whereas McIntosh *et al.*[22] developed four voxel models including a 30 g male mouse, 22 g female mouse, 22 g pregnant mouse, and 0.5 g mouse fetus.

In 2004, Segars *et al.*[14] reported on the first hybrid mouse model, termed MOBY, constructed using MR images of a male C57BL/6 mouse. This model is very popular and has been widely used for research encompassing a wide variety of applications including but not limited to imaging physics and radiation dosimetry. A number of models have been derived from the MOBY model. A voxel model of MOBY was devised by researchers from Japan Atomic Energy Agency (JAEA).[25] Keenan *et al.*,[21] derived 25, 30, and 35 g voxel mouse models whereas Larsson *et al.*[24] derived three voxel-based tumor-bearing mouse models from MOBY. More recently, Xie and Zaidi[27] modified the original MOBY model to derive 17 voxel mouse models of various body sizes. More recently, a deformable mouse atlas with adaptable body weight and body poses was also reported.[63,64]

3.B. Rat models

The rat is prized as a preeminent laboratory animal in biomedical research owing to the similarities between the

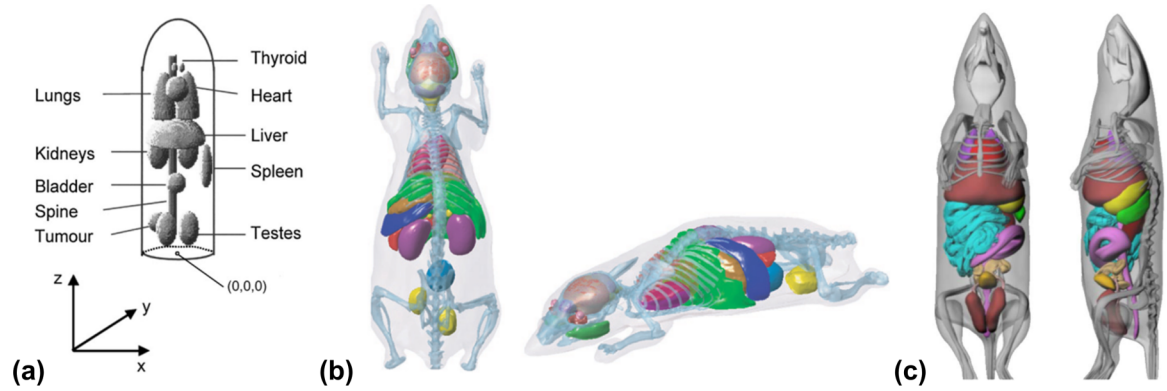

FIG. 5. (a) The stylized mouse model of Hindof *et al.* (Ref. 13), (b) the voxel mouse model of Dogdas *et al.* (Ref. 19) (Digimouse), and (c) the hybrid mouse model of Segars *et al.* (Ref. 14) (MOBY). [Reproduced with permission from C. Hindorf, M. Ljungberg, and S. E. Strand, "Evaluation of parameters influencing S values in mouse dosimetry," J. Nucl. Med. **45**, 1960–1965 (2004). Copyright © 2004 SNMMI; W. P. Segars, B. M. Tsui, E. C. Frey, G. A. Johnson, and S. S. Berr, "Development of a 4-D digital mouse phantom for molecular imaging research," Mol. Imaging Biol. **6**, 149–159 (2004). Copyright © 2004 Springer; and B. Dogdas, D. Stout, A. F. Chatziioannou, and R. M. Leahy, "Digimouse: A 3D whole body mouse atlas from CT and cryosection data," Phys. Med. Biol. **52**, 577–587 (2007). Copyright © 2007 IOP Publishing.]

rodent genome and the human genome, and the easy and less costly breeding of rats in the laboratory. The most popular rat strains for laboratory research include the Wistar rat, Sprague-Dawley (SD) rat, and Fischer rat. Figure 6 compares various types of representative computational rat models including stylized,[33] voxel-based,[39] and hybrid[43] category of models.

A number of simplified stylized rat models have been developed based on estimated anatomic data (mostly SD rat specimens) for a variety of applications, including electromagnetic field (EMF) dosimetry[31,37] and ionizing radiation dosimetry.[5,12,33,38] A number of voxel-based rat models were developed from either CT, MRI, or cryosection. Segars *et al.*[14] developed the first hybrid male Wistar rat model, known as ROBY, that was modified to create new models and extensively used by various groups for different purposes. Zhang *et al.*[43] and Xie *et al.*,[5] of Huazhong University of Science and Technology (HUST) reported on a hybrid model based on cryosection images of a SD rat specimen.

In 1997, Burkhardt *et al.*[28] and Lapin and Allen[29] developed voxel-based rat models based on MR and CT images, respectively, for electromagnetic modeling applications. Mason *et al.*[30] reported on a 370 g voxel-based rat model for EMF dosimetry. Similarly, other voxel-based rat models based on CT and MRI were developed for dosimetric analysis in experiments of electromagnetic exposure.[34,35] Most voxel-based rat models were developed from CT scans. This includes models based on a 248 g SD rat,[17] a 310 g Wistar rat,[39] three Fischer 344 rats having 126, 263, and 359 g body weight,[32] and three rats having weights of 115, 314, and 472 g produced by the National Institute of Information and Communications Technology (NICT).[44] Other models were developed based

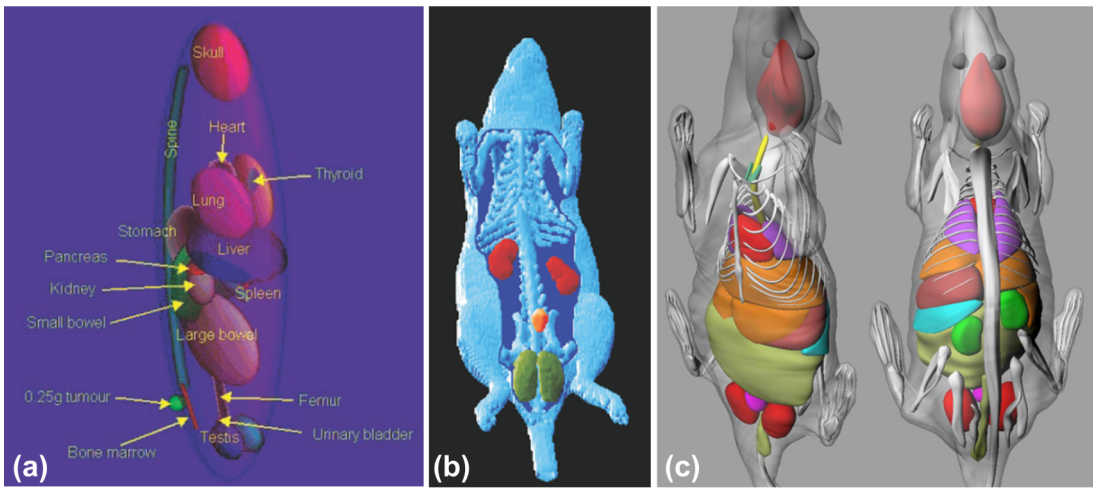

FIG. 6. Comparison between different categories of computational rat models showing (a) the stylized rat model of Konijnenberg *et al.* (Ref. 33), (b) the voxel mouse model of Peixoto *et al.* (Ref. 39), and (c) the hybrid mouse model of Zhang *et al.* (Ref. 43). [Reproduced with permission from M. W. Konijnenberg, M. Bijster, E. P. Krenning, and M. de Jong, "A stylized computational model of the rat for organ dosimetry in support of preclinical evaluations of peptide receptor radionuclide therapy with ^{90}Y, ^{111}In, or ^{177}Lu," J. Nucl. Med. **45**, 1260–1269 (2004). Copyright © 2004 SNMMI; P. Peixoto, J. Vieira, H. Yoriyaz, and F. Lima, "Photon and electron absorbed fractions calculated from a new tomographic rat model," Phys. Med. Biol. **53**, 5343–5355 (2008). Copyright © 2008 IOP Publishing; and G. Zhang, T. Xie, H. Bosmans, and Q. Liu, "Development of a rat computational phantom using boundary representation method for Monte Carlo simulation in radiological imaging," Proc. IEEE **97**, 2006–2014 (2009). Copyright © 2009 IEEE.]

on MRI, including voxel rat models SD rat[42] and pregnant Fischer 344 rat.[41]

Kainz *et al.*[36] developed four voxel SD rat models from microtome slice pictures having 567, 479, 252, and 228 g body weight whereas Wu *et al.*[40] developed a 156 g SD rat model from cryosection images. This model was later modified to incorporate a detailed model of liver lobes to make it suitable for in radionuclide therapy research for the treatment of hepatocellular carcinoma.[46]

A number of voxel-based models have developed based on the ROBY model, including five Wistar rat models with weights ranging between 200 and 600 with a step of 100 g (Ref. 21) and models of Brown Norway rat.[45] More recently, Xie and Zaidi[47,48] devised a series of voxel rat models at various ages, and with different degrees of emaciation and obesity by modifying the original ROBY model. Figure 7 shows the developed mild, moderate, severely emaciated, and the obese rat models in comparison to the normal-weight rat model.

3.C. Computational models of other animals

Few other small and larger animals were developed and served as reference animal models in biomedical and radiation protection research. Figure 8 shows representative models of the stylized deer model of ICRP,[38] a voxel trout model,[50] and a hybrid canine model.[53] The body of the adult reference deer is roughly represented by an ellipsoid with dimensions of

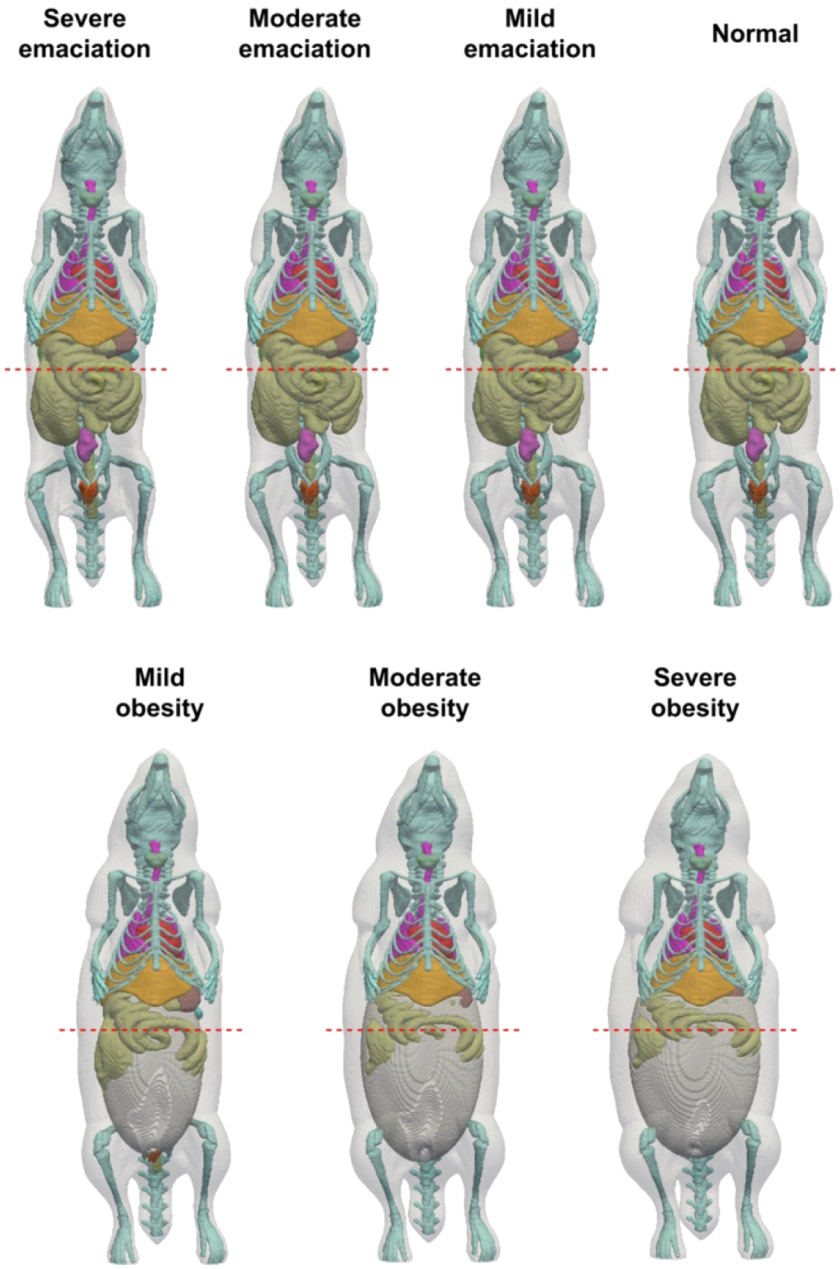

FIG. 7. 3D visualization of the rat models with different degrees of emaciation and obesity. [Reproduced with permission from T. Xie and H. Zaidi, "Effect of emaciation and obesity on small-animal internal radiation dosimetry for positron-emitting radionuclides," Eur. J. Nucl. Med. Mol. Imaging **40**, 1748–1759 (2013). Copyright © 2009 Springer.]

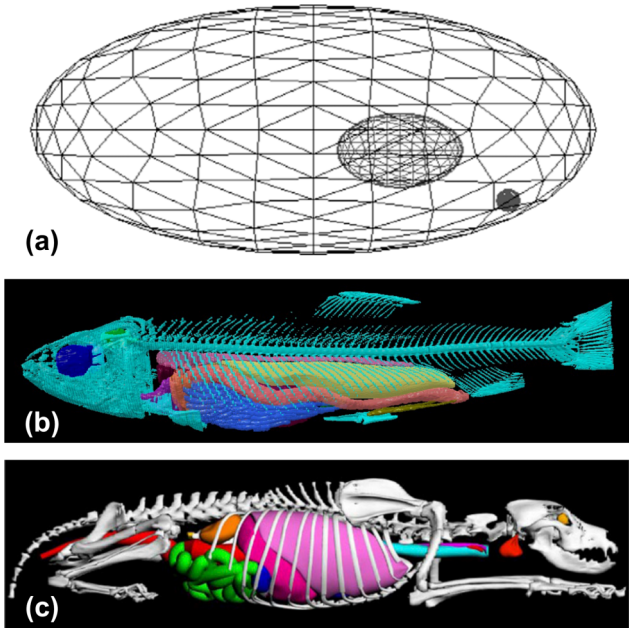

FIG. 8. (a) The stylized deer model of ICRP publication 108 (Ref. 38), (b) the voxel trout model of Hess *et al.* (Ref. 50), and (c) the hybrid canine model of Padilla *et al.* (Ref. 53). [Reproduced with permission from ICRP, "Publication 108: Environmental protection: The concept and use of reference animals and plants," Ann. ICRP **38**, 25–37 (2008). Copyright © 2008 ICRP; C. Hess, "Monte Carlo derived absorbed fractions in a voxelized model of a rainbow trout," Oregon State University (2014). Copyright @ 2014 Oregon State University; and L. Padilla, C. Lee, R. Milner, A. Shahlaee, and W. E. Bolch, "Canine anatomic phantom for preclinical dosimetry in internal emitter therapy," J. Nucl. Med. **49**, 446–452 (2008). Copyright © 2008 SNMMI.]

130×60×60 cm. The ICRP in its publication 108 dedicated to environmental protection, developed a series of stylized animal models including a 754 g crab model, 1260 g trout model, a 31.4 g frog model, a 1310 g flatfish model, a 0.589 g bee model, a 245 kg deer model, a 1260 g duck model, and a 5.24 g earthworm model to study the effect of radiation exposure of wild animals. Mason *et al.*[30] developed voxel models of a 20 kg pigmy goat, a 7.1 kg rhesus monkey, and another monkey model based on MR images. Based on CT and MRI scans, researchers from Oregon State University developed voxel models for a 464 g Dungeness crab, a 658 g Rainbow trout, and a 1024 g Pleuronectid flatfish.[50,52,65] A voxel-based frog model was also developed using cryosection images.[51] Toivonen *et al.*[54] and Wake *et al.*,[55] developed voxel-based pig and rabbit models, respectively, for finite-difference time-domain (FDTD) simulation of radio frequency (RF) radiation dosimetry. The University of Florida constructed a stylized model, a voxel model, and a hybrid model of the same 24 kg Hound cross canine specimen.[53]

4. SIMULATION TOOLS USED WITH THE COMPUTATIONAL MODELS

Computational phantoms are commonly used as surrogates to characterize the anatomy of actual animals and are integrated within simulation tools to simulate radiation transport inside the animal body, thus providing patterns of radiation interactions and estimated distributions of energy deposition. For ionizing radiation dosimetry applications (e.g., internal radiation dosimetry of radiotracers, imaging physics research involving imaging modalities such as CT, PET, and SPECT, and external beam radiotherapy applications), statistical simulation-based Monte Carlo modeling techniques are the most commonly used approaches because of their capability to account for all aspects of particle interactions within 3D heterogeneous media.[66,67] A number of popular Monte Carlo codes (e.g., EGS4, MCNP, and GEANT4) were developed to simulate the transport of multiple particles (electrons, positrons, photons, protons, etc.) in medical radiation physics and have improved geometry capabilities enabling to simulate complex configurations of computational models. These are currently available in the public domain as open-source software and widely used by the medical physics community. The EGS Monte Carlo system[68] was first developed by Stanford Linear Accelerator Center based on the MORTRAN programming language for the purpose of simulating the coupled transport of electrons and photons in an arbitrary geometry. The MCNP system[69] was developed in Los Alamos National Laboratory based on the FORTRAN programming language and is capable of simulating particle interactions of 34 different types of particles at various energies. The GEANT4 software package[70] developed by the European Organization for Nuclear Research is written in c++ language and many GEANT4-based computational tools have been devised for analyzing interactions of particles with matter. In addition, the Monte Carlo method has also been used extensively for simulating light propagation in biological tissues because of its capabilities to solve radiative transport equations for both forward and inverse problems of light–tissue interactions.[71]

Many numerical tools have been developed in computational electromagnetism including finite-element methods (FEMs) with adaptive unstructured meshes,[72] the boundary-element methods (BEMs) which discretize only interfaces between homogeneous materials,[73] and the FDTD algorithm which divides space and time into a regular grid and simulates the time evolution of Maxwell's equations[74] for calculation of the amount of energy absorbed by the organism from nonionizing radiation exposures. Commercial or open-source software packages (such as CST, XFDTD, and MEEP)[75–77] have incorporated these computational electromagnetic methods and used for bio-electromagnetics research using computational human or animal models.

5. APPLICATIONS OF ANIMAL COMPUTATIONAL MODELS

Figure 9 shows the increasing number of annual peer-reviewed publications reporting on the use of computational animal models demonstrating the growing applications of computational models in biomedical research. From 2004 to 2014, research studies reporting on the use of computational animal models have increased by a factor of 5.5. This graph is based on publications on the Web of Science™ quoting the computational animal models summarized in Table I. To

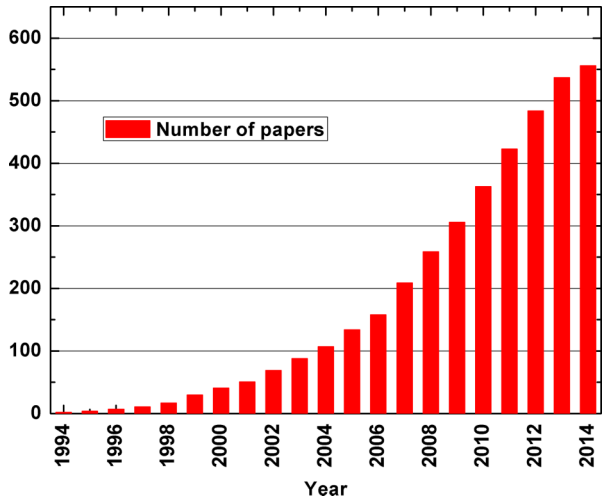

FIG. 9. Exponential growth of the number of annual peer-reviewed publications reporting on the development and/or usage of computational animal models.

illustrate the use of computational models for simulation-based medical physics research, this section summarizes studies published since 1995 covering contributions to ionizing and nonionizing radiation dosimetry and medical imaging physics.

5.A. Ionizing radiation dosimetry

Ionizing radiation dosimetry using animal models typically involves organ dose quantities and absorbed dose distributions for external x-ray sources or internal radiotracer sources. In the Medical Internal Radiation Dose (MIRD) schema, the absorbed fraction (AF) and *S*-values are the basic measures of internal radiation dose. The former describes the proportion of energy deposited in the target organ released in source organs, whereas the latter describes the equivalent dose rate in the target organ per unit activity in the source organ. *S*-values depend on the decay scheme of the radionuclide, the type, energy, and yield of emitted radiation per nuclear transformation, the mass of the target organ, and the preconstructed anatomical computational model. These measures are used for the calculation of individual organ absorbed doses for interested animal specimen. Databases of AFs and *S*-values for animals, such as mouse, rat, frog, and canine, of monoenergetic photons and electrons and common radionuclides including F-18, P-32, Cu-64, Y-90, In-111, I-124, I-131, Sm-153, Pm-149, Ho-166, Lu-177, and Re-188, have been reported by various groups.[11,15,17,18,21,24,27,33,39,45,46,49,53,78–82] These were largely adopted for calculation of organ absorbed dose and dosimetry of radionuclide-labeled compounds in preclinical experiments.[83–95] These computational models were also integrated in comparative Monte Carlo-based simulations studies investigating patterns of uptake and biodistribution data of radiopharmaceuticals for the purpose of dose estimation in molecular radiotherapy and diagnostic nuclear medical imaging procedures.[96–107] For external exposure to ionizing radiation, few studies reported on the calculation of organ dose conversion coefficients for small animals under ideal irradiation conditions (left lateral, right lateral, dorsal–ventral, ventral–dorsal, and isotropic irradiation directions),[26,40] therapeutic irradiation conditions,[23] and diagnostic imaging x-ray irradiations.[60] A number of studies have evaluated factors influencing small animal internal radiation dosimetry.[13,25,108] More recently, Xie and Zaidi assessed the effect of age[47,48] and various conditions of emaciation and obesity[52] on small animal internal radiation dosimetry. The discrepancies between small animal dosimetric results when using stylized, voxel, and hybrid models were also studied and reported in numerous contributions.[5,109,110] Overall, the ratios of self-absorbed *S*-factors ranged between 0.6 and 1.0 when comparing hybrid and voxel-based models and between 0.2 and 1.6 when comparing stylized and voxel-based models. The input parameters used for the simulations, such as model resolution, organ segmentation, tissue density, and spatial sampling, proved to have a substantial influence on small animal absorbed dose calculations when using hybrid models.[111] For *S*-values, significant discrepancies reaching even 160% were observed between the different models for some organs. These discrepancies could not be directly correlated with mass variations.

5.B. Nonionizing radiation dosimetry

For nonionizing radiation, animal models were widely used in experiments involving the assessment of the biological effects of RF-based devices, such as electromagnetic waves, wireless local area networks, high-field MRI, as well as personal cellular phones. The growing interest in studying nonionizing radiation effects is reflected by the steadily increasing usage of various nonionizing radiation emitting devices. Early studies on bioeffects of RFs on animal and human bodies were performed by Mason *et al.*,[112] where computer-based heterogeneous rat, monkey, goat, and adult man models were developed and used to determine the localized specific-absorption-rate (SAR) values that can be compared to empirical measurements in animal experiments. Following this study, animal SAR values were calculated and reported for mouse, rat, rabbit, and pig under RF exposures of 800 MHz–2 GHz cellular phone electromagnetic fields.[22,36,44,54,113–123] Dosimetry calculations were performed for the exposure of mice and rabbit to 2.45 GHz WiFi frequencies.[124–129] Fig. 10 shows the modeled RF exposure system with the developed computational pregnant mouse model for SAR calculations.[22] The SAR levels and the peak temperature increase in the fetus were determined to be around 14% and 45% lower than the values in the dam, respectively. Trakic *et al.*[130] developed a FDTD-based thermal model to evaluate the temperature elevation in SD rat due to electromagnetic energy deposition in high-field MRI with field strengths ranging from 11.75 to 23.5 T (0.5–1 GHz).

5.C. Medical imaging physics

Another important application of animal models is medical imaging physics, where computational models realistically

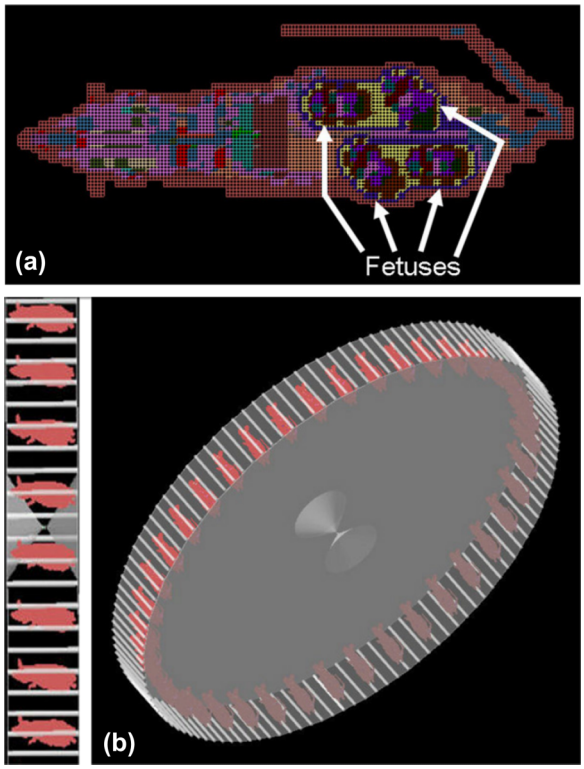

FIG. 10. (a) A pregnant mouse model and (b) simulated RF exposure system. [Reproduced with permission from R. L. McIntosh, L. Deppeler, M. Oliva, J. Parente, and F. Tambuwala, "Comparison of radiofrequency exposure of a mouse dam and foetuses at 900 MHz," Phys. Med. Biol. **55**, N111–N122 (2010). Copyright © 2010 IOP Publishing.]

mimic the anatomic structure and physicochemical characteristics of laboratory animals. These are commonly combined with simulation tools accounting for all physical aspects involved in the image acquisition process and characteristics of the imaging system to generate a simulated dataset that closely mimic clinical and experimental studies. The known features of computational models and simulated datasets provide precise information enabling to evaluate the impact of physical degrading factors inherent to the imaging process,[131–135] assess different design concepts and performance of medical imaging systems,[136–150] and advance the development and validation of new image segmentation,[151–155] registration,[156–161] reconstruction,[162–167] and processing techniques.[168–175] Likewise, the Digimouse and MOBY models served as optically heterogeneous virtual subjects for light propagation calculations to assess the impact of various parameters involved in optical molecular imaging techniques[176–184] and to evaluate the performance of BLT (Refs. 185–195) and FMT (Refs. 196–206) tomographic imaging systems. Two examples of studies carried out in the authors' lab (Geneva University Hospital) are briefly discussed below to illustrate the use of computational models in medical imaging physics research. Prasad and Zaidi[134] realistically modeled the LabPET™ small animal PET scanner using the GEANT4-based Monte Carlo simulation platform to simulate particle transport within the animal model and the PET scanner, thus enabling to obtain simulated projection data of total events and to assess the magnitude, distribution, and origin of the scatter component in small animal PET. Figure 11 shows the setup for Monte Carlo simulation of single- and multiple-subject small animal PET imaging configurations. Gutierrez and Zaidi[157] developed an automatic atlas-guided method for analysis of small animal PET data through deformable registration to the Digimouse anatomical mouse model and used the MOBY model to generate simulated PET images and CT images of mice of various sizes to validate the proposed methodology. Figure 12 shows the activity map, attenuation map, segmented image, simulated x-ray projection image, CT image, and ^{18}F-FDG PET image of the MOBY model.

6. SUMMARY

Similar to the development of human phantoms, the progress in computational anatomical models for animals evolved from mathematical objects based on simplified geometrical shapes modeling the body and internal organs, through voxel models extracted from medical imaging data of real subjects, and more recently hybrid computational models that combine in an elegant way easy to standardize mathematical equations of stylized models and the anatomical realism of voxel models. Over the last decade, the degree of realism and complexity of these computational models has significantly increased. To date, more than 120 computational animal models covering 15 different species have been painstakingly created to respond to research requirements in ionizing and nonionizing radiation dosimetry, multimodality imaging physics and instrumentation, and image analysis and

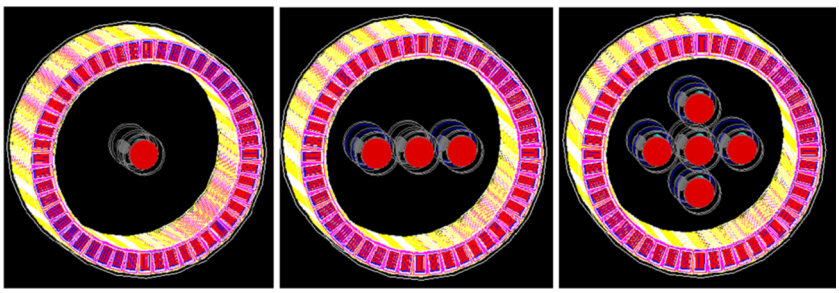

FIG. 11. Setup for Monte Carlo simulation of single- and multiple-subject imaging configurations in small animal PET scanning. [Reproduced with permission from R. Prasad and H. Zaidi, "Scatter characterization and correction for simultaneous multiple small-animal PET imaging," Mol. Imaging Biol. **16**, 199–209 (2014). Copyright © 2014 Springer.]

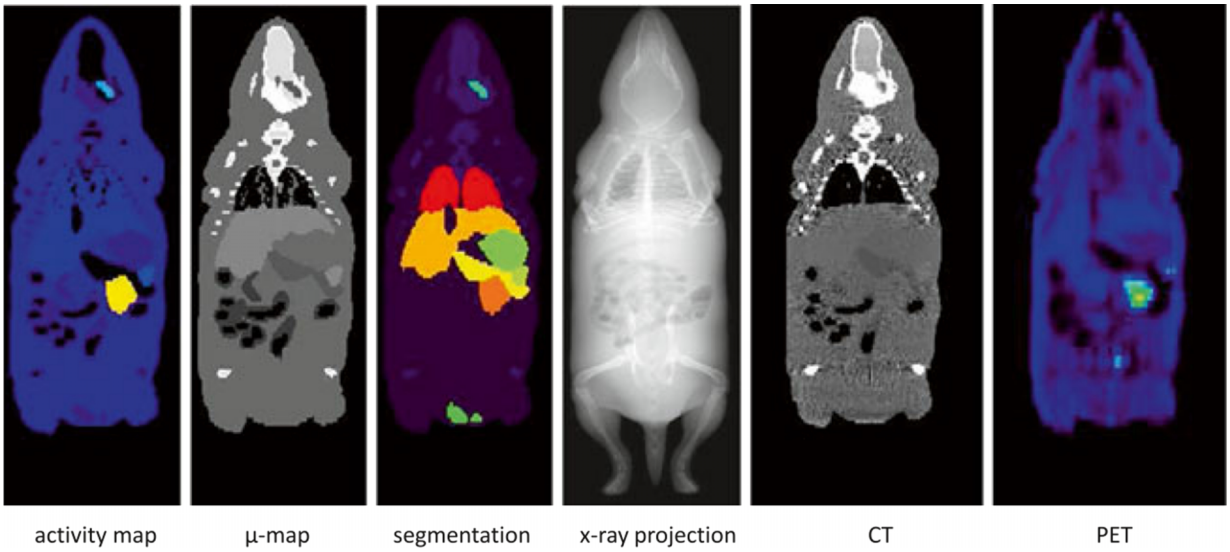

FIG. 12. Coronal views showing from left to right: the activity map, attenuation map, segmented image highlighting the different organs and tissues, simulated x-ray projection image, CT image, and ^{18}F-FDG PET image of the MOBY model. [Reproduced with permission from D. F. Gutierrez and H. Zaidi, "Automated analysis of small animal PET studies through deformable registration to an atlas," Eur. J. Nucl. Med. Mol. Imaging **39**, 1807–1820 (2012). Copyright © 2012 Springer.]

processing. The pros and cons of stylized, voxel, and hybrid models can be briefly elaborated under three general themes: anatomical fidelity, geometrical flexibility, and compatibility with simulation tools.

With respect to the anatomical realism achieved by computational models, voxel models constructed from tomographic images of animals and hybrid models using advanced boundary representation techniques provide considerable improvement over first-generation stylized models. The unrealistic anatomy of stylized models causes substantial deviation in terms of dosimetric results under various conditions.[5] However, the anatomical fidelity of voxel models depends on the voxel size keeping in mind that the cube-shaped surface was reported to cause the voxel size effect in radiation dosimetry.[4] Conversely, hybrid and stylized models have smooth organ surfaces and can easily be adjusted to describe typical organ deformation during physiological cardiac and respiratory motion.

Regarding compatibility and ease of usage of anatomical models, both stylized and voxel models have the simplest geometric elements and can be easily integrated in most commercial or open-source simulation tools. However, except for tetrahedral-mesh-based models,[207] most of the hybrid models using B-splines, NURBS, and polygon meshes cannot be directly incorporated in popular Monte Carlo simulation packages. Two solutions were used to cope with the computational compatibility of hybrid models. The first method consists in generating a corresponding voxel model from the hybrid model using voxelization tools, and then uses the voxelized hybrid model as input for simulations. The second option involves modifying the simulation tool to add capabilities enabling to handle the processing of complex geometries. The new version of GEANT4 package was developed to directly implement computer-aided design (CAD)-based polygon-mesh models for general-purpose Monte Carlo particle transport simulations.[208]

Another issue that should be carefully considered is the usage of reference animal models. The concept of reference model is widely accepted in the field of human radiation protection and the ICRP proposed a series of reference animal models for environmental protection. However, significant individual variations have been reported for different animal subjects, which results in divergences in terms of calculated radiation dose even for animal models of the same origin having close weights.[27,111] In the context of preclinical research based on animal models, the assessment of the geometrical variability of experimental specimens should be performed to assist the selection of the most appropriate computational model for radiation dosimetry.

There are many advantages for using computational models and simulation tools over physical phantoms or real animals. One of the main advantages of computational phantoms is that the user has the possibility to define the desired properties in terms of anatomy and physiological functions, which enables him to generate data under controlled conditions where the ground truth is known. The latter could then serve as reference enabling the assessment of the performance of imaging devices, accuracy of image analysis, and reconstruction techniques or radiation dosimetry calculations. Another advantage is that computational phantoms are nonradioactive "willing participants" that can straightforwardly be modified to emulate various anatomies and physiological conditions, thus providing a large population of animals for medical physics research.[4] Conducting research with real animals is always expensive and complex involving clearing ethical aspects and solving difficult practical and logistic issues.

A fundamental question that has to be addressed in this context is what are the criteria motivating the choice of the most appropriate model for a given application? In preclinical

research focusing on radiation dosimetry calculations, the organ mass of the animal model and the distance between organs are the most important factors influencing self-absorbed *S*-values and cross-absorbed *S*-values, respectively. Therefore, the animal model having the most similar anatomical parameters, including body weight, length, age, and strain, as the actual animal would be the most appropriate one. Stylized models provide a mean value representation of small animals and would be suitable for large-scale radiation dosimetry studies (such as environmental radiation protection) where the accuracy of dosimetry calculations is limited by anatomic variations between subjects. For advanced molecular imaging applications involving dynamic studies considering cardiac and respiratory motion, and body movement, hybrid models would be most appropriate. In preclinical research, real animals are commonly used to investigate the biological effects of radiation and for basic and translational research studies where the role played by either physical or computational phantoms is very limited.

There is growing interest in targeted molecular therapy and molecular imaging with pharmacological radioactive agents, where computational animal models play an important role in the validation of new imaging techniques, enabling a reduction in the number of animals used in preclinical research.

7. FUTURE PERSPECTIVES

Currently, more than 70% of total animal models are voxel models while only four hybrid animal models have been reported for male C57BL/6 mouse, male Wistar rat, male SD rat, and Hound cross canine, respectively. Advanced boundary representation techniques endue the development of hybrid models presenting with a realistic description of animal anatomy and smooth organ surfaces free of voxel effect, with the additional capability of easy transformation of organ position and shape for anatomic matching of experimental subjects. With the development of advanced simulation and computer graphics tools, it is not far-fledged to see more hybrid animal models for various species and to witness an explosion of applications of hybrid models in radiation dosimetry and multimodality imaging research. Meanwhile, since mice served as the most important laboratory animal for preclinical studies, the development of dosimetric databases for mice of different strains, weights, and ages could be valuable for assessing rodent-specific radiation dose from the multitude of imaging experiments typically used to address basic research questions. Meanwhile, with the rapid development of microradiation therapy small animal conformal irradiators,[209] computational small animal models will be useful for preclinical studies enabling to generate data for translational research.

ACKNOWLEDGMENTS

This work was supported by the Swiss National Science Foundation under Grant No. SNSF 31003A-149957 and Geneva Cancer League.

[a]Author to whom correspondence should be addressed. Electronic mail: habib.zaidi@hcuge.ch; Telephone: +41 22 372 7258; Fax: +41 22 372 7169.

[1]H. Zaidi and X. G. Xu, "Computational anthropomorphic models of the human anatomy: The path to realistic Monte Carlo modeling in radiological sciences," Annu. Rev. Biomed. Eng. **9**, 471–500 (2007).
[2]X. G. Xu, "An exponential growth of computational phantom research in radiation protection, imaging, and radiotherapy: A review of the fifty-year history," Phys. Med. Biol. **59**, R233–R302 (2014).
[3]H. Zaidi and B. M. Tsui, "Review of computational anthropomorphic anatomical and physiological models," Proc. IEEE **97**, 1938–1953 (2009).
[4]X. G. Xu and K. F. Eckerman, *Handbook of Anatomical Models for Radiation Dosimetry* (CRC, Boca Raton, FL, 2010).
[5]T. Xie, G. Zhang, Y. Li, and Q. Liu, "Comparison of absorbed fractions of electrons and photons using three kinds of computational phantoms of rat," Appl. Phys. Lett. **97**, 033702 (2010).
[6]T. E. Hui, D. R. Fisher, J. A. Kuhn, L. E. Williams, and C. Nourigat, "A mouse model for calculating cross-organ beta doses from yttrium-90-labeled immunoconjugates," Cancer **73**, 951–957 (1994).
[7]S. J. Kennel, M. Stabin, H. Yoriyaz, M. Brechbiel, and S. Mirzadeh, "Treatment of lung tumor colonies with ^{90}Y targeted to blood vessels: Comparison with the α-particle emitter ^{213}Bi," Nucl. Med. Biol. **26**, 149–157 (1999).
[8]M. Dhenain, S. W. Ruffins, and R. E. Jacobs, "Three-dimensional digital mouse atlas using high-resolution MRI," Dev. Biol. **232**, 458–470 (2001).
[9]A. Flynn, A. Green, R. Pedley, G. Boxer, and R. Boden, "A mouse model for calculating the absorbed beta-particle dose from ^{131}I-and ^{90}Y-labeled immunoconjugates, including a method for dealing with heterogeneity in kidney and tumor," Radiat. Res. **156**, 28–35 (2001).
[10]W. Jianqing and O. Fujiwara, "A novel setup for small animal exposure to near fields to test biological effects of cellular telephones," IEICE Trans. Commun. **84**, 3050–3059 (2001).
[11]K. S. Kolbert, T. Watson, C. Matei, S. Xu, and J. A. Koutcher, "Murine S factors for liver, spleen, and kidney," J. Nucl. Med. **44**, 784–791 (2003).
[12]T. Funk, M. Sun, and B. H. Hasegawa, "Radiation dose estimate in small animal SPECT and PET," Med. Phys. **31**, 2680–2686 (2004).
[13]C. Hindorf, M. Ljungberg, and S. E. Strand, "Evaluation of parameters influencing S values in mouse dosimetry," J. Nucl. Med. **45**, 1960–1965 (2004).
[14]W. P. Segars, B. M. Tsui, E. C. Frey, G. A. Johnson, and S. S. Berr, "Development of a 4-D digital mouse phantom for molecular imaging research," Mol. Imaging Biol. **6**, 149–159 (2004).
[15]W. H. Miller, C. Hartmann-Siantar, D. Fisher, M.-A. Descalle, and T. Daly, "Evaluation of beta-absorbed fractions in a mouse model for ^{90}Y, ^{188}Re, ^{166}Ho, ^{149}Pm, ^{64}Cu, and ^{177}Lu radionuclides," Cancer Biother.Radiopharm. **20**, 436–449 (2005).
[16]Y. Sato, H. Yamabayashi, and T. Nakamura, "Internal dose distribution of ^{90}Y beta-ray source implanted in a small phantom simulating a mouse," Radioisotopes **57**, 385–391 (2008).
[17]M. G. Stabin, T. E. Peterson, G. E. Holburn, and M. A. Emmons, "Voxel-based mouse and rat models for internal dose calculations," J. Nucl. Med. **47**, 655–659 (2006).
[18]A. Bitar, A. Lisbona, P. Thedrez, C. S. Maurel, and D. Le Forestier, "A voxel-based mouse for internal dose calculations using Monte Carlo simulations (MCNP)," Phys. Med. Biol. **52**, 1013–1025 (2007).
[19]B. Dogdas, D. Stout, A. F. Chatziioannou, and R. M. Leahy, "Digimouse: A 3D whole body mouse atlas from CT and cryosection data," Phys. Med. Biol. **52**, 577–587 (2007).
[20]X. Zhang, J. Tian, J. Feng, S. Zhu, and G. Yan, "An anatomical mouse model for multimodal molecular imaging," in *Annual International Conference of the IEEE Engineering in Medicine and Biology Society* (IEEE, Minneapolis, MN, 2009), pp. 5817–5820.
[21]M. A. Keenan, M. G. Stabin, W. P. Segars, and M. J. Fernald, "RADAR realistic animal model series for dose assessment," J. Nucl. Med. **51**, 471–476 (2010).
[22]R. L. McIntosh, L. Deppeler, M. Oliva, J. Parente, and F. Tambuwala, "Comparison of radiofrequency exposure of a mouse dam and foetuses at 900 MHz," Phys. Med. Biol. **55**, N111–N122 (2010).
[23]J. C. Chow, M. K. Leung, P. E. Lindsay, and D. A. Jaffray, "Dosimetric variation due to the photon beam energy in the small-animal irradiation: A Monte Carlo study," Med. Phys. **37**, 5322–5329 (2010).
[24]E. Larsson, M. Ljungberg, S. E. Strand, and B. A. Jönsson, "Monte Carlo calculations of absorbed doses in tumours using a modified MOBY mouse

phantom for pre-clinical dosimetry studies," Acta Oncol. **50**, 973–980 (2011).
[25]A. Mohammadi and S. Kinase, "Influence of voxel size on specific absorbed fractions and S-values in a mouse voxel phantom," Radiat. Prot. Dosim. **143**, 258–263 (2011).
[26]X. Zhang, X. Xie, J. Cheng, J. Ning, and Y. Yuan, "Organ dose conversion coefficients based on a voxel mouse model and MCNP code for external photon irradiation," Radiat. Prot. Dosim. **148**, 9–19 (2012).
[27]T. Xie and H. Zaidi, "Monte Carlo-based evaluation of S-values in mouse models for positron-emitting radionuclides," Phys. Med. Biol. **58**, 169–182 (2013).
[28]M. Burkhardt, Y. Spinelli, and N. Kuster, "Exposure setup to test effects of wireless communications systems on the CNS," Health Phys. **73**, 770–778 (1997).
[29]G. Lapin and C. Allen, "Requirements for accurate anatomical imaging of the rat for electromagnetic modeling," in *Proceedings of the 19th Annual International Conference of the IEEE Engineering in Medicine and Biology Society* (IEEE, Chicago, IL, 1997), Vol. 6, pp. 2480–2483.
[30]P. Mason, J. Ziriax, W. Hurt, and J. D'Andrea, "3-dimensional models for EMF dosimetry," in *Electricity and Magnetism in Biology and Medicine* (Springer, New York, NY, 1999), pp. 291–294.
[31]C. Chou, K. Chan, J. McDougall, and A. Guy, "Development of a rat head exposure system for simulating human exposure to RF fields from handheld wireless telephones," Bioelectromagnetics **20**, 75–92 (1999).
[32]S. Watanabe, A. Mukoyama, K. Wake, Y. Yamanaka, and T. Uno, "Microwave exposure setup for a long-term *in vivo* study," in *Proceedings of the International Symposium on Antennas and Propagation Japan* (ISAP, Fukuoka, 2000), Vol. 1, pp. 225–228.
[33]M. W. Konijnenberg, M. Bijster, E. P. Krenning, and M. de Jong, "A stylized computational model of the rat for organ dosimetry in support of preclinical evaluations of peptide receptor radionuclide therapy with ^{90}Y, ^{111}In, or ^{177}Lu," J. Nucl. Med. **45**, 1260–1269 (2004).
[34]P. Leveque, C. Dale, B. Veyret, and J. Wiart, "Dosimetric analysis of a 900-MHz rat head exposure system," IEEE Trans. Microwave Theory Tech. **52**, 2076–2083 (2004).
[35]F. Schönborn, K. Poković, and N. Kuster, "Dosimetric analysis of the carousel setup for the exposure of rats at 1.62 GHz," Bioelectromagnetics **25**, 16–26 (2004).
[36]W. Kainz, N. Nikoloski, W. Oesch, V. Berdiñas-Torres, and J. Fröhlich, "Development of novel whole-body exposure setups for rats providing high efficiency, national toxicology program (NTP) compatibility and well-characterized exposure," Phys. Med. Biol. **51**, 5211–5229 (2006).
[37]V. Lopresto, R. Pinto, A. De Vita, S. Mancini, and P. Galloni, "Exposure setup to study potential adverse effects at GSM 1800 and UMTS frequencies on the auditory systems of rats," Radiat. Prot. Dosim. **123**, 473–482 (2007).
[38]ICRP, "Publication 108: Environmental protection: The concept and use of reference animals and plants," Ann. ICRP **38**, 25–37 (2008).
[39]P. Peixoto, J. Vieira, H. Yoriyaz, and F. Lima, "Photon and electron absorbed fractions calculated from a new tomographic rat model," Phys. Med. Biol. **53**, 5343–5355 (2008).
[40]L. Wu, G. Zhang, Q. Luo, and Q. Liu, "An image-based rat model for Monte Carlo organ dose calculations," Med. Phys. **35**, 3759–3764 (2008).
[41]J. Wang, O. Fujiwara, K. Wake, and S. Watanabe, "Dosimetry evaluation for pregnant and fetus rats in a near-field exposure system of 1.95-GHz cellular phones," IEEE Microwave Wireless Compon. Lett. **18**, 260–262 (2008).
[42]F. Pain, M. Dhenain, H. Gurden, A. Routier, and F. Lefebvre, "A method based on Monte Carlo simulations and voxelized anatomical atlases to evaluate and correct uncertainties on radiotracer accumulation quantitation in beta microprobe studies in the rat brain," Phys. Med. Biol. **53**, 5385–5404 (2008).
[43]G. Zhang, T. Xie, H. Bosmans, and Q. Liu, "Development of a rat computational phantom using boundary representation method for Monte Carlo simulation in radiological imaging," Proc. IEEE **97**, 2006–2014 (2009).
[44]T. Arima, H. Watanabe, K. Wake, H. Masuda, and S. Watanabe, "Local exposure system for rats head using a figure-8 loop antenna in 1500-MHz band," IEEE Trans. Biomed. Eng. **58**, 2740–2747 (2011).
[45]E. Larsson, M. Ljungberg, L. Mårtensson, R. Nilsson, and J. Tennvall, "Use of Monte Carlo simulations with a realistic rat phantom for examining the correlation between hematopoietic system response and red marrow absorbed dose in Brown Norway rats undergoing radionuclide therapy with ^{177}Lu-and ^{90}Y-BR96 mAbs," Med. Phys. **39**, 4434–4443 (2012).
[46]T. Xie, Q. Liu, and H. Zaidi, "Evaluation of S-values and dose distributions for ^{90}Y, ^{131}I, ^{166}Ho, and ^{188}Re in seven lobes of the rat liver," Med. Phys. **39**, 1462–1472 (2012).
[47]T. Xie and H. Zaidi, "Age-dependent small-animal internal radiation dosimetry," Mol. Imaging **12**, 364–375 (2013).
[48]T. Xie and H. Zaidi, "Effect of emaciation and obesity on small-animal internal radiation dosimetry for positron-emitting radionuclides," Eur. J. Nucl. Med. Mol. Imaging **40**, 1748–1759 (2013).
[49]E. Caffrey and K. Higley, "Creation of a voxel phantom of the ICRP reference crab," J. Environ. Radioact. **120**, 14–18 (2013).
[50]C. Hess, "Monte Carlo derived absorbed fractions in a voxelized model of a rainbow trout," Master's Thesis, Oregon State University (2014).
[51]S. Kinase, "Voxel-based frog phantom for internal dose evaluation," J. Nucl. Sci. Technol. **45**, 1049–1052 (2008).
[52]E. A. Caffrey, "Improvements in the dosimetric models of selected benthic organisms," Master's thesis, Oregon State University, 2012.
[53]L. Padilla, C. Lee, R. Milner, A. Shahlaee, and W. E. Bolch, "Canine anatomic phantom for preclinical dosimetry in internal emitter therapy," J. Nucl. Med. **49**, 446–452 (2008).
[54]T. Toivonen, T. Toivo, R. Pitkääho, L. Puranen, and M. Silfverhuth, "Setup and dosimetry for exposing anaesthetised pigs *in vivo* to 900 MHz GSM mobile phone fields," Bioelectromagnetics **29**, 363–370 (2008).
[55]K. Wake, H. Hongo, S. Watanabe, M. Taki, and Y. Kamimura, "Development of a 2.45-GHz local exposure system for *in vivo* study on ocular effects," IEEE Trans. Microwave Theory Tech. **55**, 588–596 (2007).
[56]H. Zaidi and I. El Naqa, "PET-guided delineation of radiation therapy treatment volumes: A survey of image segmentation techniques," Eur. J. Nucl. Med. Mol. Imaging **37**, 2165–2187 (2010).
[57]J. M. Boone, O. Velazquez, and S. R. Cherry, "Small-animal x-ray dose from micro-CT," Mol. Imaging **3**, 149–158 (2004).
[58]C. T. Badea, M. Drangova, D. W. Holdsworth, and G. A. Johnson, "*In vivo* small-animal imaging using micro-CT and digital subtraction angiography," Phys. Med. Biol. **53**, R319–R350 (2008).
[59]N. L. Ford, M. M. Thornton, and D. W. Holdsworth, "Fundamental image quality limits for microcomputed tomography in small animals," Med. Phys. **30**, 2869–2877 (2003).
[60]R. Taschereau, P. L. Chow, and A. F. Chatziioannou, "Monte Carlo simulations of dose from microCT imaging procedures in a realistic mouse phantom," Med. Phys. **33**, 216–224 (2006).
[61]S. K. Carlson, K. L. Classic, C. E. Bender, and S. J. Russell, "Small animal absorbed radiation dose from serial micro-computed tomography imaging," Mol. Imaging Biol. **9**, 78–82 (2007).
[62]C. T. Badea, B. Fubara, L. W. Hedlund, and G. A. Johnson, "4-D micro-CT of the mouse heart," Mol. Imaging **4**, 110–116 (2005).
[63]A. Joshi, A. Chaudhari, C. Li, D. Shattuck, J. Dutta, R. Leahy, and A. Toga, "Posture matching and elastic registration of a mouse atlas to surface topography range data," in *International Symposium on Biomedical Imaging: From Nano to Macro, ISBI'09* (IEEE, 2009), pp. 366–369.
[64]H. Wang, D. B. Stout, and A. F. Chatziioannou, "A deformable atlas of the laboratory mouse," Mol. Imaging Biol. **17**, 18–28 (2014).
[65]E. Ruedig, E. Caffrey, C. Hess, and K. Higley, "Monte Carlo derived absorbed fractions for a voxelized model of Oncorhynchus mykiss, a rainbow trout," Radiat. Environ. Biophys. **53**, 581–587 (2014).
[66]H. Zaidi, "Relevance of accurate Monte Carlo modeling in nuclear medical imaging," Med. Phys. **26**, 574–608 (1999).
[67]D. Rogers, "Fifty years of Monte Carlo simulations for medical physics," Phys. Med. Biol. **51**, R287–R301 (2006).
[68]I. Kawrakow and D. Rogers, The EGSnrc code system: Monte Carlo simulation of electron and photon transport, 2014, available at http://irs.inms.nrc.ca/software/egsnrc/.
[69]J. F. Briesmeister, MCNP—A general Monte Carlo code for neutron and photon transport, LA-7396–M, 1986.
[70]S. Agostinelli, J. Allison, K. a. Amako, J. Apostolakis, and H. Araujo, "GEANT4—A simulation toolkit," Nucl. Instrum. Methods Phys. Res., Sect. A **506**, 250–303 (2003).
[71]C. Zhu and Q. Liu, "Review of Monte Carlo modeling of light transport in tissues," J. Biomed. Opt. **18**, 050902–050903 (2013).
[72]M. N. Sadiku, *Numerical Techniques in Electromagnetics* (CRC, Boca Raton, FL, 2000).
[73]S. M. Rao, D. Wilton, and A. W. Glisson, "Electromagnetic scattering by surfaces of arbitrary shape," IEEE Trans. Antennas Propag. **30**, 409–418 (1982).

[74]A. Taflove and S. C. Hagness, *Computationai Electrodynamics* (Artech House, Norwood, 2000).
[75]A. F. Oskooi, D. Roundy, M. Ibanescu, P. Bermel, and J. D. Joannopoulos, "MEEP: A flexible free-software package for electromagnetic simulations by the FDTD method," Comput. Phys. Commun. **181**, 687–702 (2010).
[76]CST, Computer simulation technology, https://www.cst.com/, accessed 2015.
[77]REMCOM, http://www.remcom.com, accessed 2015.
[78]A. Bitar, A. Lisbona, and M. Bardies, "S-factor calculations for mouse models using Monte-Carlo simulations," Q. J. Nucl. Med. Mol. Imaging **51**, 343–351 (2007).
[79]S. Kinase, "Monte Carlo simulations of photon absorbed fractions in a frog voxel phantom," Proc. IEEE **97**, 2086–2097 (2009).
[80]S. Kinase, A. Mohammadi, M. Takahashi, K. Saito, and M. Zankl, "Computer simulations for internal dosimetry using voxel models," Radiat. Prot. Dosim. **146**, 191–194 (2011).
[81]E. Larsson, S. E. Strand, M. Ljungberg, and B. A. Jonsson, "Mouse S-factors based on Monte Carlo simulations in the anatomical realistic Moby phantom for internal dosimetry," Cancer Biother. Radiopharm. **22**, 438–442 (2007).
[82]T. Xie, D. Han, Y. Liu, W. Sun, and Q. Liu, "Skeletal dosimetry in a voxel-based rat phantom for internal exposures to photons and electrons," Med. Phys. **37**, 2167–2178 (2010).
[83]M. Luna-Gutierrez, G. Ferro-Flores, B. Ocampo-Garcia, N. Jimenez-Mancilla, and E. Morales-Avila, "^{177}Lu-labeled monomeric, dimeric and multimeric RGD peptides for the therapy of tumors expressing a(v) b(3) integrins," J. Labelled Compd. Radiopharm. **55**, 140–148 (2012).
[84]J. M. Bertho, N. Synhaeve, H. Miloudi, J. Stefani, and A. Desbree, "Absorbed radiation doses due to chronic ingestion of cesium-137 or strontium-90 by mice," Radioprotection **47**, 219–230 (2012).
[85]H. Song, K. Shahverdi, D. L. Huso, C. Esaias, and J. Fox, "Bi-213 (alpha-emitter)-antibody targeting of breast cancer metastases in the neu-N transgenic mouse model," Cancer Res. **68**, 3873–3880 (2008).
[86]L. Melendez-Alafort, A. Nadali, E. Zangoni, A. Banzato, and M. Rondina, "Biokinetic and dosimetric studies of Re-188-hyaluronic acid: A new radiopharmaceutical for treatment of hepatocellular carcinoma," Nucl. Med. Biol. **36**, 693–701 (2009).
[87]J. Rodriguez-Cortes, C. A. De Murphy, G. Ferro-Flores, M. Pedraza-Lopez, and E. Murphy-Stack, "Biokinetics and dosimetry with Lu-177-DOTA-TATE in athymic mice with induced pancreatic malignant tumours: Preclinical studies," Radiat. Eff. Defects Solids **162**, 791–796 (2007).
[88]E. R. Balkin, F. Jia, W. H. Miller, and M. R. Lewis, "*In vitro* evaluation of targeted antisense Lu-177 radiotherapy," Anticancer Res. **31**, 3143–3149 (2011).
[89]E. Fischer, J. Gruenberg, S. Cohrs, A. Hohn, and K. Waldner-Knogler, "L1-CAM-targeted antibody therapy and ^{177}Lu-radioimmunotherapy of disseminated ovarian cancer," Int. J. Cancer **130**, 2715–2721 (2012).
[90]M. S. Muthuswamy, P. L. Roberson, and D. J. Buchsbaum, "A mouse bone marrow dosimetry model," J. Nucl. Med. **39**, 1243–1247 (1998).
[91]D. J. Green, N. N. Orgun, J. C. Jones, M. D. Hylarides, and J. M. Pagel, "A preclinical model of CD38-pretargeted radioimmunotherapy for plasma cell malignancies," Cancer Res. **74**, 1179–1189 (2014).
[92]E. Frampas, C. Maurel, P. R.-L. Saec, T. Mauxion, and A. Faivre-Chauvet, "Pretargeted radioimmunotherapy of colorectal cancer metastases: Models and pharmacokinetics predict influence of the physical and radiochemical properties of the radionuclide," Eur. J. Nucl. Med. Mol. Imaging **38**, 2153–2164 (2011).
[93]J. Lazewatsky, Y. H. Ding, D. Onthank, P. Silva, and E. Solon, "Radiation dose to abdominal organs of the mouse due to Y-90 in the urinary bladder," Cancer Biother.Radiopharm. **18**, 413–419 (2003).
[94]G. Sgouros, M. Stabin, Y. Erdi, G. Akabani, and C. Kwok, "Red marrow dosimetry for radiolabeled antibodies that bind to marrow, bone, or blood components," Med. Phys. **27**, 2150–2164 (2000).
[95]G. Liu, S. Dou, G. Mardirossian, J. He, and S. Zhang, "Successful radiotherapy of tumor in pretargeted mice by Re-188-radiolabeled phosphorodiamidate morpholino oligomer, a synthetic DNA analogue," Clin. Cancer Res. **12**, 4958–4964 (2006).
[96]E. R. Balkin, D. Liu, F. Jia, V. C. Ruthengael, and S. M. Shaffer, "Comparative biodistributions and dosimetry of Lu-177 DOTA-anti-bcl-2-PNA-Tyr(3)-octreotate and Lu-177 DOTA-Tyr(3)-octreotate in a mouse model of B-cell lymphoma/leukemia," Nucl. Med. Biol. **41**, 36–42 (2014).
[97]J. N. Bryan, F. Jia, H. Mohsin, G. Sivaguma, and W. H. Miller, "Comparative uptakes and biodistributions of internalizing vs. noninternalizing copper-64 radioimmunoconjugates in cell and animal models of colon cancer," Nucl. Med. Biol. **32**, 851–858 (2005).
[98]B. Cambien, P. R. Franken, A. Lamit, T. Mauxion, and P. Richard-Fiardo, "(TcO4-)-Tc-99m-, auger-mediated thyroid stunning: Dosimetric requirements and associated molecular events," PLoS One **9**, e92729 (2014).
[99]S. M. Goddu, A. Bishayee, L. G. Bouchet, W. E. Bolch, and D. V. Rao, "Marrow toxicity of P-33- versus P-32-orthophosphate: Implications for therapy of bone pain and bone metastases," J. Nucl. Med. **41**, 941–951 (2000).
[100]S. Kinase, S. Matsuhashi, and K. Saito, "Interspecies scaling of self-organ dose from a voxel mouse to voxel humans," Nucl. Technol. **168**, 154–157 (2009).
[101]M. Melis, E. Vegt, M. W. Konijnenberg, M. de Visser, and M. Bijster, "Nephrotoxicity in mice after repeated imaging using In-111-labeled peptides," J. Nucl. Med. **51**, 973–977 (2010).
[102]H. Mohsin, F. Jia, J. N. Bryan, G. Sivaguru, and C. S. Cutler, "Comparison of pretargeted and conventional CC49 radioimmunotherapy using (149)pm, Ho-166, and Lu-177," Bioconjugate Chem. **22**, 2444–2452 (2011).
[103]R. Taschereau and A. F. Chatziioannou, "Monte Carlo simulations of absorbed dose in a mouse phantom from 18-fluorine compounds," Med. Phys. **34**, 1026–1036 (2007).
[104]S. Thompson, B. Ballard, Z. Jiang, E. Revskaya, and N. Sisay, "Ho-166 and Y-90 labeled 6D2 monoclonal antibody for targeted radiotherapy of melanoma: Comparison with Re-188 radiolabel," Nucl. Med. Biol. **41**, 276–281 (2014).
[105]O. Ugur, L. Kostakoglu, E. T. Hui, D. R. Fisher, and K. Garmestani, "Comparison of the targeting characteristics of various radioimmunoconjugates for radioimmunotherapy of neuroblastoma: Dosimetry calculations incorporating cross-organ beta doses," Nucl. Med. Biol. **23**, 1–8 (1996).
[106]O. Ugur, A. M. Scott, L. Kostakoglu, T. E. Hui, and M. E. Masterson, "Calculated and TLD-based absorbed dose estimates for I-131-labeled 3F8 monoclonal-antibody in a human neuroblastoma xenograft nude-mouse model," Nucl. Med. Biol. **22**, 87–93 (1995).
[107]L. Aranda-Lara, G. Ferro-Flores, E. Azorín-Vega, F. de María Ramírez, N. Jiménez-Mancilla, B. Ocampo-García, C. Santos-Cuevas, and K. Isaac-Olivé, "Synthesis and evaluation of Lys 1 (α, γ-Folate) Lys 3 (177 Lu-DOTA)-Bombesin (1-14) as a potential theranostic radiopharmaceutical for breast cancer," Appl. Radiat. Isot. **107**, 214–219 (2015).
[108]S. Boutaleb, J.-P. Pouget, C. Hindorf, A. Pelegrin, and J. Barbet, "Impact of mouse model on preclinical dosimetry in targeted radionuclide therapy," Proc. IEEE **97**, 2076–2085 (2009).
[109]A. Mohammadi, S. Kinase, and K. Saito, "Evaluation of absorbed doses in voxel-based and simplified models for small animals," Radiat. Prot. Dosim. **150**, 283–291 (2012).
[110]T. Xie and H. Zaidi, "Assessment of S values in stylized and voxel-based rat models for positron-emitting radionuclides," Mol. Imaging Biol. **15**, 542–551 (2013).
[111]T. Mauxion, J. Barbet, J. Suhard, J.-P. Pouget, and M. Poirot, "Improved realism of hybrid mouse models may not be sufficient to generate reference dosimetric data," Med. Phys. **40**, 052501 (11pp.) (2013).
[112]P. A. Mason, W. D. Hurt, T. J. Walters, J. A. D'Andrea, and P. Gajsek, "Effects of frequency, permittivity, and voxel size on predicted specific absorption rate values in biological tissue during electromagnetic-field exposure," IEEE Trans. Microwave Theory Tech. **48**, 2050–2058 (2000).
[113]A. Hirata, H. Masuda, Y. Kanai, R. Asai, and O. Fujiwara, "Computational modeling of temperature elevation and thermoregulatory response in the brains of anesthetized rats locally exposed at 1.5 GHz," Phys. Med. Biol. **56**, 7639–7657 (2011).
[114]E. Lopez-Martin, J. C. Bregains, F. J. Jorge-Barreiro, J. L. Sebastian-Franco, and E. Moreno-Piquero, "An experimental set-up for measurement of the power absorbed from 900 MHz GSM standing waves by small animals, illustrated by application to picrotoxin-treated rats," Prog. Electromagn. Res. **87**, 149–165 (2008).
[115]N. Prochnow, T. Gebing, K. Ladage, D. Krause-Finkeldey, and A. El Ouardi, "Electromagnetic field effect or simply stress? Effects of UMTS exposure on hippocampal longterm plasticity in the context of procedure related hormone release," PLoS One **6**, e19437 (2011).
[116]L. Puranen, T. Toivo, T. Toivonen, R. Pitkaeaeho, and A. Turunen, "Space efficient system for whole-body exposure of unrestrained rats to 900 MHz electromagnetic fields," Bioelectromagnetics **30**, 120–128 (2009).
[117]K. Wake, A. Mukoyama, S. Watanabe, Y. Yamanaka, and T. Uno, "An exposure system for long-term and large-scale animal bioassay of 1.5-GHz

digital cellular phones," IEEE Trans. Microwave Theory Tech. **55**, 343–350 (2007).
[118]J. Wang, O. Fujiwara, H. Kawai, K. Wake, and S. Watanabe, "Development and dosimetry analysis of a 2-GHz whole-body exposure setup for unrestrained pregnant and newborn rats," IEEE Trans. Microwave Theory Tech. **56**, 2008–2013 (2008).
[119]J. Wang, W. Liao, H. Kawai, K. Wake, and S. Watanabe, "Performance and validation of a broadband-multigeneration exposure system for unconstrained rats," IEEE Trans. Microwave Theory Tech. **61**, 326–334 (2013).
[120]J. Q. Wang, M. Fujita, O. Fujiwara, K. Wake, and S. Watanabe, "Uncertainty evaluation of an *in vivo* near-field exposure setup for testing biological effects cellular phones," IEEE Trans. Electromagn. Compat. **48**, 545–551 (2006).
[121]J. Q. Wang and O. Fujiwara, "Realizing highly localized exposure in small animals with absorbing material covered holder to test biological effects of 1.5 GHz cellular telephones," IEICE Trans. Commun. **E86B**, 1660–1665 (2003).
[122]J. Q. Wang, T. Saito, and O. Fujiwara, "Uncertainty evaluation of dosimetry due to plastic holder for restraining small animal in *in vivo* near field exposure setup," IEEE Trans. Electromagn. Compat. **46**, 263–267 (2004).
[123]L. Yang, D. Hao, S. Wu, R. Zhong, and Y. Zeng, "SAR and temperature distribution in the rat head model exposed to electromagnetic field radiation by 900 MHz dipole antenna," Australas. Phys. Eng. Sci. Med. **36**, 251–257 (2013).
[124]A. Hirata and O. Fujiwara, "Modeling time variation of blood temperature in a bioheat equation and its application to temperature analysis due to RF exposure," Phys. Med. Biol. **54**, N189–N196 (2009).
[125]A. Hirata, H. Sugiyama, M. Kojima, H. Kawai, and Y. Yamashiro, "Computational model for calculating body-core temperature elevation in rabbits due to whole-body exposure at 2.45 GHz," Phys. Med. Biol. **53**, 3391–3404 (2008).
[126]T. Oizumi, I. Laakso, A. Hirata, O. Fujiwara, and S. Watanabe, "FDTD analysis of temperature elevation in the lens of human and rabbit models due to near-field and far-field exposures at 2.45 GHz," Radiat. Prot. Dosim. **155**, 284–291 (2013).
[127]R. Pinto, V. Lopresto, P. Galloni, C. Marino, and S. Mancini, "Dosimetry of a set-up for the exposure of newborn mice to 2.45-GHz WiFi frequencies," Radiat. Prot. Dosim. **140**, 326–332 (2010).
[128]J. Q. Wang, O. Fujiwara, and T. Ono, "Dosimetry evaluation of a whole body exposure setup for small animal at 2.45 GHz," IEICE Trans. Commun. **E85B**, 2963–2965 (2002).
[129]T. Wu, A. Hadjem, M.-F. Wong, A. Gati, O. Picon, and J. Wiart, "Whole-body new-born and young rats' exposure assessment in a reverberating chamber operating at 2.4 GHz," Phys. Med. Biol. **55**, 1619–1630 (2010).
[130]A. Trakic, S. Crozier, and F. Liu, "Numerical modelling of thermal effects in rats due to high-field magnetic resonance imaging (0.5-1 GHz)," Phys. Med. Biol. **49**, 5547–5558 (2004).
[131]A. Koenik, M. T. Madsen, and J. J. Sunderland, "GATE simulations of small animal SPECT for determination of scatter fraction as a function of object size," IEEE Trans. Nucl. Sci. **59**, 1887–1891 (2012).
[132]A. Konik, T. Koesters, M. T. Madsen, and J. J. Sunderland, "Evaluation of attenuation and scatter correction requirements as a function of object size in small animal PET imaging," IEEE Trans. Nucl. Sci. **58**, 2308–2314 (2011).
[133]A. Konik, M. T. Madsen, and J. J. Sunderland, "GATE simulations of human and small animal PET for determination of scatter fraction as a function of object size," IEEE Trans. Nucl. Sci. **57**, 2558–2563 (2010).
[134]R. Prasad and H. Zaidi, "Scatter characterization and correction for simultaneous multiple small-animal PET imaging," Mol. Imaging Biol. **16**, 199–209 (2014).
[135]R. Prasad and H. Zaidi, "A cone-shaped phantom for assessment of small animal PET scatter fraction and count rate performance," Mol. Imaging Biol. **14**, 561–571 (2012).
[136]A. Sisniega, W. Zbijewski, A. Badal, I. S. Kyprianou, and J. W. Stayman, "Monte Carlo study of the effects of system geometry and antiscatter grids on cone-beam CT scatter distributions," Med. Phys. **40**, 051915 (19pp.) (2013).
[137]E. Brard and D. Brasse, "Axially oriented crystal geometry applied to small-animal PET system: A proof of concept," IEEE Trans. Nucl. Sci. **60**, 1471–1477 (2013).
[138]T. Funk, P. Despres, W. C. Barber, K. S. Shah, and B. H. Hasegawa, "A multipinhole small animal SPECT system with submillimeter spatial resolution," Med. Phys. **33**, 1259–1268 (2006).
[139]S. C. Huang, D. Truong, H. M. Wu, A. F. Chatziioannou, and W. Shao, "An internet-based 'kinetic imaging system' (KIS) for MicroPET," Mol. Imaging Biol. **7**, 330–341 (2005).
[140]R. Van Holen, B. Vandeghinste, K. Deprez, and S. Vandenberghe, "Design and performance of a compact and stationary microSPECT system," Med. Phys. **40**, 112501 (11pp.) (2013).
[141]F. Boisson, C. J. Wimberley, W. Lehnert, D. Zahra, and T. Pham, "NEMA NU 4-2008 validation and applications of the PET-SORTEO Monte Carlo simulations platform for the geometry of the Inveon PET preclinical scanner," Phys. Med. Biol. **58**, 6749–6763 (2013).
[142]S. Branco, S. Jan, and P. Almeida, "Monte Carlo simulations in small animal PET imaging," Nucl. Instrum. Methods Phys. Res., Sect. A **580**, 1127–1130 (2007).
[143]W. Branderhorst, F. van der Have, B. Vastenhouw, M. A. Viergever, and F. J. Beekman, "Murine cardiac images obtained with focusing pinhole SPECT are barely influenced by extra-cardiac activity," Phys. Med. Biol. **57**, 717–732 (2012).
[144]C. L. Chen, Y. Wang, J. J. S. Lee, and B. M. W. Tsui, "Integration of SimSET photon history generator in GATE for efficient Monte Carlo simulations of pinhole SPECT," Med. Phys. **35**, 3278–3284 (2008).
[145]M. C. Goorden and F. J. Beekman, "High-resolution tomography of positron emitters with clustered pinhole SPECT," Phys. Med. Biol. **55**, 1265–1277 (2010).
[146]C. Lartizien, C. Kuntner, A. L. Goertzen, A. C. Evans, and A. Reilhac, "Validation of PET-SORTEO Monte Carlo simulations for the geometries of the MicroPET R4 and Focus 220 PET scanners," Phys. Med. Biol. **52**, 4845–4862 (2007).
[147]O. Lee and J. C. Ye, "Joint sparsity-driven non-iterative simultaneous reconstruction of absorption and scattering in diffuse optical tomography," Opt. Express **21**, 26589–26604 (2013).
[148]G. S. P. Mok, Y. Du, Y. Wang, E. C. Frey, and B. M. W. Tsui, "Development and validation of a Monte Carlo simulation tool for multi-pinhole SPECT," Mol. Imaging Biol. **12**, 295–304 (2010).
[149]G. S. P. Mok, Y. Wang, and B. M. W. Tsui, "Quantification of the multiplexing effects in multi-pinhole small animal SPECT: A simulation study," IEEE Trans. Nucl. Sci. **56**, 2636–2643 (2009).
[150]G. S. P. Mok, J. Yu, Y. Du, Y. Wang, and B. M. W. Tsui, "Evaluation of a multi-pinhole collimator for imaging small animals with different sizes," Mol. Imaging Biol. **14**, 60–69 (2012).
[151]M. Baiker, J. Milles, J. Dijkstra, T. D. Henning, and A. W. Weber, "Atlas-based whole-body segmentation of mice from low-contrast micro-CT data," Med. Image Anal. **14**, 723–737 (2010).
[152]J. Cheng-Liao and J. Qi, "Segmentation of mouse dynamic PET images using a multiphase level set method," Phys. Med. Biol. **55**, 6549–6569 (2010).
[153]D. Clark, A. Badea, Y. Liu, G. A. Johnson, and C. T. Badea, "Registration-based segmentation of murine 4D cardiac micro-CT data using symmetric normalization," Phys. Med. Biol. **57**, 6125–6145 (2012).
[154]A. Khmelinskii, H. C. Groen, M. Baiker, M. de Jong, and B. P. F. Lelieveldt, "Segmentation and visual analysis of whole-body mouse skeleton microSPECT," PLoS One **7**, e48976 (2012).
[155]R. Maroy, R. Boisgard, C. Comat, V. Frouin, and P. Cathier, "Segmentation of rodent whole-body dynamic PET images: An unsupervised method based on voxel dynamics," IEEE Trans. Med. Imaging **27**, 342–354 (2008).
[156]C. T. Badea, E. Schreibmann, and T. Fox, "A registration based approach for 4D cardiac micro-CT using combined prospective and retrospective gating," Med. Phys. **35**, 1170–1179 (2008).
[157]D. F. Gutierrez and H. Zaidi, "Automated analysis of small animal PET studies through deformable registration to an atlas," Eur. J. Nucl. Med. Mol. Imaging **39**, 1807–1820 (2012).
[158]S. C. Moore, S. Southekal, M.-A. Park, S. J. McQuaid, and M. F. Kijewski, "Improved regional activity quantitation in nuclear medicine using a new approach to correct for tissue partial volume and spillover effects," IEEE Trans. Med. Imaging **31**, 405–416 (2012).
[159]H. Wang, D. B. Stout, and A. F. Chatziioannou, "Mouse atlas registration with non-tomographic imaging modalities—A pilot study based on simulation," Mol. Imaging Biol. **14**, 408–419 (2012).
[160]H. Wang, D. B. Stout, and A. F. Chatziioannou, "Estimation of mouse organ locations through registration of a statistical mouse atlas with micro-CT images," IEEE Trans. Med. Imaging **31**, 88–102 (2012).

[161]H. M. Wu, M. C. Kreissl, H. R. Schelbert, W. Ladno, and M. Prins, "First-pass angiography in mice using FDG-PET: A simple method of deriving the cardiovascular transit time without the need of region-of-interest drawing," IEEE Trans. Nucl. Sci. **52**, 1311–1315 (2005).
[162]J. Cabello and M. Rafecas, "Comparison of basis functions for 3D PET reconstruction using a Monte Carlo system matrix," Phys. Med. Biol. **57**, 1759–1777 (2012).
[163]J. Cheng-Liao and J. Qi, "PET image reconstruction with anatomical edge guided level set prior," Phys. Med. Biol. **56**, 6899–6918 (2011).
[164]D. D'Ambrosio, G. Fiacchi, M. Marengo, S. Boschi, and S. Fanti, "Reconstruction of images using accurate system point spread function modeling: Effects on parametric images," J. Mech. Med. Biol. **10**, 73–94 (2010).
[165]A. Gaitanis, G. Kontaxakis, G. Spyrou, G. Panayiotakis, and G. Tzanakos, "PET image reconstruction: A stopping rule for the MLEM algorithm based on properties of the updating coefficients," Comput. Med. Imaging Graphics **34**, 131–141 (2010).
[166]E. Quan and D. S. Lalush, "A faster ordered-subset convex algorithm for iterative reconstruction in a rotation-free micro-CT system," Phys. Med. Biol. **54**, 1061–1072 (2009).
[167]A. Salomon, B. Goldschmidt, R. Botnar, F. Kiessling, and V. Schulz, "A self-normalization reconstruction technique for PET scans using the positron emission data," IEEE Trans. Med. Imaging **31**, 2234–2240 (2012).
[168]T. Dumouchel and R. A. deKemp, "Analytical-based partial volume recovery in mouse heart imaging," IEEE Trans. Nucl. Sci. **58**, 110–120 (2011).
[169]T. Dumouchel, S. Thorn, M. Kordos, J. DaSilva, and R. S. B. Beanlands, "A three-dimensional model-based partial volume correction strategy for gated cardiac mouse PET imaging," Phys. Med. Biol. **57**, 4309–4334 (2012).
[170]A. L. Kesner, M. Dahlbom, S.-C. Huang, W.-A. Hsueh, and B. S. Pio, "Semiautomated analysis of small-animal PET data," J. Nucl. Med. **47**, 1181–1186 (2006).
[171]A. Khmelinskii, M. Baiker, E. L. Kaijzel, J. Chen, and J. H. C. Reiber, "Articulated whole-body atlases for small animal image analysis: Construction and applications," Mol. Imaging Biol. **13**, 898–910 (2011).
[172]R. Maroy, R. Boisgard, C. Comtat, B. Jego, and Y. Fontyn, "Quantitative organ time activity curve extraction from rodent PET images without anatomical prior," Med. Phys. **37**, 1507–1517 (2010).
[173]Y. Su and K. I. Shoghi, "Single-input-dual-output modeling of image-based input function estimation," Mol. Imaging Biol. **12**, 286–294 (2010).
[174]Y. Su, M. J. Welch, and K. I. Shoghi, "The application of maximum likelihood factor analysis (MLFA) with uniqueness constraints on dynamic cardiac microPET data," Phys. Med. Biol. **52**, 2313–2334 (2007).
[175]Y. Zan, R. Boutchko, Q. Huang, B. Li, and K. Chen, "Fast direct estimation of the blood input function and myocardial time activity curve from dynamic SPECT projections via reduction in spatial and temporal dimensions," Med. Phys. **40**, 092503 (10pp.) (2013).
[176]A. Kavanagh, A. Olivo, R. Speller, and B. Vojnovic, "Feasibility testing of a pre-clinical coded aperture phase contrast imaging configuration using a simple fast Monte Carlo simulator," Biomed. Opt. Express **5**, 93–105 (2014).
[177]D. Yang, X. Chen, S. Ren, X. Qu, and J. Tian, "Influence investigation of a void region on modeling light propagation in a heterogeneous medium," Appl. Opt. **52**, 400–408 (2013).
[178]H. Shen and G. Wang, "A study on tetrahedron-based inhomogeneous Monte Carlo optical simulation," Biomed. Opt. Express **2**, 44–57 (2011).
[179]H. Shen and G. Wang, "A tetrahedron-based inhomogeneous Monte Carlo optical simulator," Phys. Med. Biol. **55**, 947–962 (2010).
[180]D. Yang, X. Chen, Z. Peng, X. Wang, and J. Ripoll, "Light transport in turbid media with non-scattering, low-scattering and high absorption heterogeneities based on hybrid simplified spherical harmonics with radiosity model," Biomed. Opt. Express **4**, 2209–2223 (2013).
[181]Y. Lu and A. F. Chatziioannou, "A parallel adaptive finite element method for the simulation of photon migration with the radiative-transfer-based model," Commun. Numer. Methods Eng. **25**, 751–770 (2009).
[182]W. Li, H. Yi, Q. Zhang, D. Chen, and J. Liang, "Extended finite element method with simplified spherical harmonics approximation for the forward model of optical molecular imaging," Comput. Math. Methods Med. **2012**, 1–10.
[183]O. Lee, J. M. Kim, Y. Bresler, and J. C. Ye, "Compressive diffuse optical tomography: Noniterative exact reconstruction using joint sparsity," IEEE Trans. Med. Imaging **30**, 1129–1142 (2011).
[184]J. Chen and X. Intes, "Time-gated perturbation Monte Carlo for whole body functional imaging in small animals," Opt. Express **17**, 19566–19579 (2009).
[185]H. Dehghani, S. C. Davis, and B. W. Pogue, "Spectrally resolved bioluminescence tomography using the reciprocity approach," Med. Phys. **35**, 4863–4871 (2008).
[186]Q. Wu, J. Feng, K. Jia, and X. Wang, "Improved reconstruction quality of bioluminescent images by combining SP3 equations and bregman iteration method," Comput. Math. Methods Med. **2013**, 1–8.
[187]M. A. Naser, M. S. Patterson, and J. W. Wong, "Self-calibrated algorithms for diffuse optical tomography and bioluminescence tomography using relative transmission images," Biomed. Opt. Express **3**, 2794–2808 (2012).
[188]X. He, J. Liang, X. Wang, J. Yu, and X. Qu, "Sparse reconstruction for quantitative bioluminescence tomography based on the incomplete variables truncated conjugate gradient method," Opt. Express **18**, 24825–24841 (2010).
[189]J. Yu, F. Liu, J. Wu, L. Jiao, and X. He, "Fast source reconstruction for bioluminescence tomography based on sparse regularization," IEEE Trans. Biomed. Eng. **57**, 2583–2586 (2010).
[190]X. Chen, D. Yang, X. Qu, H. Hu, and J. Liang, "Comparisons of hybrid radiosity-diffusion model and diffusion equation for bioluminescence tomography in cavity cancer detection," J. Biomed. Opt. **17**, 066015 (2012).
[191]M. A. Naser, M. S. Patterson, and J. W. Wong, "Algorithm for localized adaptive diffuse optical tomography and its application in bioluminescence tomography," Phys. Med. Biol. **59**, 2089–2109 (2014).
[192]G. Alexandrakis, F. R. Rannou, and A. F. Chatziioannou, "Effect of optical property estimation accuracy on tomographic bioluminescence imaging: Simulation of a combined optical-PET (OPET) system," Phys. Med. Biol. **51**, 2045–2053 (2006).
[193]G. Alexandrakis, F. R. Rannou, and A. F. Chatziioannou, "Tomographic bioluminescence imaging by use of a combined optical-PET (OPET) system: A computer simulation feasibility study," Phys. Med. Biol. **50**, 4225–4241 (2005).
[194]J. Yu, X. He, G. Geng, F. Liu, and L. C. Jiao, "Hybrid multilevel sparse reconstruction for a whole domain bioluminescence tomography using adaptive finite element," Comput. Math. Methods Med. **2013**, 1–11.
[195]Y. Lv, J. Tian, W. Cong, G. Wang, and W. Yang, "Spectrally resolved bioluminescence tomography with adaptive finite element analysis: Methodology and simulation," Phys. Med. Biol. **52**, 4497–4512 (2007).
[196]X. Wang, B. Zhang, X. Cao, F. Liu, and J. Luo, "Acceleration of early-photon fluorescence molecular tomography with graphics processing units," Comput. Math. Methods Med. **2013**, 1–9.
[197]X. Liu, B. Zhang, J. Luo, and J. Bai, "Principal component analysis of dynamic fluorescence tomography in measurement space," Phys. Med. Biol. **57**, 2727–2742 (2012).
[198]S. B. Raymond, A. T. N. Kumar, D. A. Boas, and B. J. Bacskai, "Optimal parameters for near infrared fluorescence imaging of amyloid plaques in Alzheimer's disease mouse models," Phys. Med. Biol. **54**, 6201–6216 (2009).
[199]T. Correia, J. Aguirre, A. Sisniega, J. Chamorro-Servent, and J. Abascal, "Split operator method for fluorescence diffuse optical tomography using anisotropic diffusion regularisation with prior anatomical information," Biomed. Opt. Express **2**, 2632–2648 (2011).
[200]X. Liu, F. Liu, and J. Bai, "A linear correction for principal component analysis of dynamic fluorescence diffuse optical tomography images," IEEE Trans. Biomed. Eng. **58**, 1602–1611 (2011).
[201]J. Chen, V. Venugopal, and X. Intes, "Monte Carlo based method for fluorescence tomographic imaging with lifetime multiplexing using time gates," Biomed. Opt. Express **2**, 871–886 (2011).
[202]A. J. Chaudhari, S. Ahn, R. Levenson, R. D. Badawi, and S. R. Cherry, "Excitation spectroscopy in multispectral optical fluorescence tomography: Methodology, feasibility and computer simulation studies," Phys. Med. Biol. **54**, 4687–4704 (2009).
[203]J. Dutta, S. Ahn, A. A. Joshi, and R. M. Leahy, "Illumination pattern optimization for fluorescence tomography: Theory and simulation studies," Phys. Med. Biol. **55**, 2961–2982 (2010).

[204]A. Joshi, J. C. Rasmussen, E. M. Sevick-Muraca, T. A. Wareing, and J. McGhee, "Radiative transport-based frequency-domain fluorescence tomography," Phys. Med. Biol. **53**, 2069–2088 (2008).
[205]J. F. Perez-Juste Abascal, J. Aguirre, J. Chamorro-Servent, M. Schweiger, and S. Arridge, "Influence of absorption and scattering on the quantification of fluorescence diffuse optical tomography using normalized data," J. Biomed. Opt. **17**, 036013 (2012).
[206]G. Zhang, F. Liu, H. Pu, W. He, and J. Luo, "A direct method with structural priors for imaging pharmacokinetic parameters in dynamic fluorescence molecular tomography," IEEE Trans. Biomed. Eng. **61**, 986–990 (2014).
[207]Y. S. Yeom, J. H. Jeong, M. C. Han, and C. H. Kim, "Tetrahedral-mesh-based computational human phantom for fast Monte Carlo dose calculations," Phys. Med. Biol. **59**, 3173–3185 (2014).
[208]M. C. Han, C. H. Kim, J. H. Jeong, Y. S. Yeom, and S. Kim, "DagSolid: A new GEANT4 solid class for fast simulation in polygon-mesh geometry," Phys. Med. Biol. **58**, 4595–4609 (2013).
[209]S. Stojadinovic *et al.*, "MicroRT—Small animal conformal irradiator," Med. Phys. **34**, 4706–4716 (2007).